Environmental snapshots from ACE-Asia

Ralph Kahn,[1] Jim Anderson,[2] Theodore L. Anderson,[3] Tim Bates,[4] Fred Brechtel,[5] Christian M. Carrico,[6] Antony Clarke,[7] Sarah J. Doherty,[3] Ellsworth Dutton,[8] Richard Flagan,[9] Robert Frouin,[10] Hajime Fukushima,[11] Brent Holben,[12] Steve Howell,[7] Barry Huebert,[7] Anne Jefferson,[8] Haflidi Jonsson,[13] Olga Kalashnikova,[1] Jiyoung Kim,[14] Sang-Woo Kim,[15] Pinar Kus,[16] Wen-Hao Li,[1] John M. Livingston,[17] Cameron McNaughton,[7] John Merrill,[18] Sonoyo Mukai,[19] Toshiyuki Murayama,[20] Teruyuki Nakajima,[21] Patricia Quinn,[4] Jens Redemann,[22] Mark Rood,[16] Phil Russell,[23] Itaru Sano,[19] Beat Schmid,[22] John Seinfeld,[9] Nobuo Sugimoto,[24] Jian Wang,[25] Ellsworth J. Welton,[12] Jae-Gwang Won,[15] and Soon-Chang Yoon[15]

Received 8 November 2003; revised 11 February 2004; accepted 12 April 2004; published 5 October 2004.

[1] On five occasions spanning the Asian Pacific Regional Aerosol Characterization Experiment (ACE-Asia) field campaign in spring 2001, the Multiangle Imaging Spectroradiometer spaceborne instrument took data coincident with high-quality observations by instruments on two or more surface and airborne platforms. The cases capture a range of clean, polluted, and dusty aerosol conditions. With a three-stage optical modeling process, we synthesize the data from over 40 field instruments into layer-by-layer environmental snapshots that summarize what we know about the atmospheric and surface states at key locations during each event. We compare related measurements and discuss the implications of apparent discrepancies, at a level of detail appropriate for satellite retrieval algorithm and aerosol transport model validation. Aerosols within a few kilometers of the surface were composed primarily of pollution and Asian dust mixtures, as expected. Medium- and coarse-mode particle size distributions varied little among the events studied; however, column aerosol optical depth changed by more than a factor of 4, and the near-surface proportion of dust ranged between 25% and 50%. The amount of absorbing material in the submicron fraction was highest when near-surface winds crossed Beijing and the Korean Peninsula and was considerably lower for all other cases. Having simultaneous single-scattering albedo measurements at more than one wavelength would significantly reduce the

[1]Jet Propulsion Laboratory, California Institute of Technology, Pasadena, California, USA.
[2]Department of Mechanical and Aerospace Engineering, Arizona State University, Tempe, Arizona, USA.
[3]Department of Atmospheric Sciences, University of Washington, Seattle, Washington, USA.
[4]NOAA Pacific Marine Environmental Laboratory, Seattle, Washington, USA.
[5]Brechtel Manufacturing, Inc., Hayward, California, USA.
[6]Department of Atmospheric Science, Colorado State University, Fort Collins, Colorado, USA.
[7]Department of Oceanography, University of Hawaii, Honolulu, Hawaii, USA.
[8]NOAA Climate Monitoring and Diagnostics Laboratory, Boulder, Colorado, USA.
[9]Department of Chemical Engineering, California Institute of Technology, Pasadena, California, USA.
[10]Scripps Institution of Oceanography, University of California, San Diego, La Jolla, California, USA.
[11]School of High-Technology for Human Welfare, Tokai University, Nishino, Numazu, Japan.
[12]NASA Goddard Space Flight Center, Greenbelt, Maryland, USA.
[13]Center for Interdisciplinary Remotely-Piloted Aircraft Studies, Naval Postgraduate School, Marina, California, USA.
[14]Meteorological Research Institute, Korea Meteorological Administration, Seoul, South Korea.
[15]School of Earth and Environmental Sciences, Seoul National University, Seoul, South Korea.
[16]Department of Civil and Environmental Engineering, University of Illinois at Urbana-Champaign, Urbana, Illinois, USA.
[17]SRI International, Menlo Park, California, USA.
[18]Graduate School of Oceanography, University of Rhode Island, Narragansett, Rhode Island, USA.
[19]Faculty of Science and Technology, Kinki University, Higashi-Osaka, Japan.
[20]Faculty of Marine Engineering, Tokyo University of Marine Science and Technology, Tokyo, Japan.
[21]Center for Climate System Research, University of Tokyo, Tokyo, Japan.
[22]Bay Area Environmental Research Institute, Sonoma, California, USA.
[23]NASA Ames Research Center, Moffett Field, California, USA.
[24]Atmospheric Environment Division, National Institute for Environmental Studies, Tsukuba, Japan.
[25]Atmospheric Science Division, Brookhaven National Laboratory, Upton, New York, USA.

0148-0227/04/2003JD004339

remaining optical model uncertainties. The consistency of component particle microphysical properties among the five events, even in this relatively complex aerosol environment, suggests that global, satellite-derived maps of aerosol optical depth and aerosol mixture (air-mass-type) extent, combined with targeted in situ component microphysical property measurements, can provide a detailed global picture of aerosol behavior. *INDEX TERMS:* 0305 Atmospheric Composition and Structure: Aerosols and particles (0345, 4801); 0345 Atmospheric Composition and Structure: Pollution—urban and regional (0305); 0368 Atmospheric Composition and Structure: Troposphere—constituent transport and chemistry; 0394 Atmospheric Composition and Structure: Instruments and techniques; 1610 Global Change: Atmosphere (0315, 0325); *KEYWORDS:* aerosols, environmental snapshots, dust, pollution, atmospheric closure

Citation: Kahn, R., et al. (2004), Environmental snapshots from ACE-Asia, *J. Geophys. Res.*, *109*, D19S14, doi:10.1029/2003JD004339.

1. Introduction

[2] The Asian Pacific Regional Aerosol Characterization Experiment (ACE-Asia) took place over Japan, Korea, and China and the surrounding waters, in spring 2001. Over 400 researchers participated, supporting multiple instrumented aircraft, ships, and land surface environmental measuring stations [*Huebert et al.*, 2003]. One reason for bringing so many resources to bear on a single region is the possibility of simultaneously characterizing key attributes of the surface and atmosphere on scales from tens of meters to tens of kilometers. Such data allow us to grasp the aggregated contributions from many parts of the environment simultaneously, essential for studies ranging from column radiative closure [e.g., *Schmid et al.*, 2003a; *Redemann et al.*, 2003] to satellite aerosol retrieval and aerosol transport model validation.

[3] This paper is aimed at these applications, with an eye toward the longer-term goal of combining the detailed particle properties that can be obtained only from in situ measurements with the frequent, synoptic coverage possible with satellite-borne instruments. Aerosol distribution validation efforts for many transport models [e.g., *Chin et al.*, 2002; *Kinne et al.*, 2003], and satellite instruments [e.g., *Hsu et al.*, 1999; *Diner et al.*, 2001; *Remer et al.*, 2002], rely heavily on the network of Sun photometers organized by the AERONET program [*Holben et al.*, 1998]. AERONET data are of great value for statistical validation analyses because of their extensive spatial and temporal coverage, uniform data acquisition and analysis approach, and timely accessibility; they are included in this study as well. However, the detailed interpretation of AERONET data alone for these applications suffers from some limitations. (1) Surface conditions in the vicinity of most AERONET sites are not well characterized; they represent lower boundary conditions critical to quantitatively assessing satellite retrieval sensitivity. (2) Particle vertical distribution, needed for assessing retrieval sensitivity and a critical test parameter for transport models, is also unavailable for most sites. (3) The ability of the AERONET algorithm to identify thin, uniform cirrus is an issue, especially for comparing with satellite data. (4) Although AERONET measurements provide time series at a fixed point, assumptions about isotropy and homogeneity must be made to use them for assessing two-dimensional spatial variability relevant to satellite observations and to model grid boxes. (5) When discrepancies arise between AERONET observations and comparison data sets, direct meteorological measurements that may help resolve the differences are often lacking.

[4] Efforts are being made to address the limitations in the monitoring station observation suite, but for the times and places where they exist, field campaign data, such as those obtained during ACE-Asia, go a long way toward filling the gaps in this picture. The measurements studied here represent a synthesis of data taken from multiple platforms. Two aircraft participated, the National Science Foundation/National Center for Atmospheric Research (NSF/NCAR) C-130 and the Center for Interdisciplinary Remotely Piloted Aircraft Studies (CIRPAS) Twin Otter (TO), along with the National Oceanographic and Atmospheric Administration (NOAA) research vessel *Ronald H. Brown* (RB). Instrumented ground stations at Amami Island, Japan, and at Gosan on Jeju Island, Korea, also contributed coincident data. Our field sampling strategy was to fly the aircraft near the surface during satellite overpasses, so airborne Sun photometers could measure total column spectral aerosol optical thickness (AOT) corresponding to that seen by the satellite, while in situ aerosol physical and chemical experiments collected samples of boundary layer air. A minimum collection time of 30 min in a typical aerosol layer was required for some airborne instruments to obtain adequate samples. Before and/or after the near-surface legs were flown, the aircraft performed vertical profiles that yielded atmospheric structure. When possible, upper level aerosol layers identified in the profiles were sampled during subsequent level-leg traverses. In many cases we were able to target aircraft operations to the vicinity of a surface station.

[5] We focus on five occasions during ACE-Asia when the Multiangle Imaging Spectroradiometer (MISR) flying aboard the NASA Earth Observing System's Terra satellite [*Diner et al.*, 1998], took data over a 400-km-wide swath coincident with high-quality, quantitative observations by two or more participating surface and airborne platforms (Table 1). In four cases each, the C-130 and TO made measurements within the MISR field of view; for two of these, the two research aircraft flew in close proximity. The RB made observations coincident with MISR on three occasions, once in close proximity to the C-130, and once within a few hundred kilometers of the TO. The Gosan surface station fell within the MISR field of view on 16 April, with the TO nearby, and on 2 May, when the C-130 was in the immediate vicinity. The Amami surface station is

Table 1. MISR Multiplatform Coincident Events During the ACE-Asia Campaign[a]

Platform	Notes
	4 April 2001, Oki and Amami Islands
MISR	orbit 6884, path 112, 0214:12 UTC at block 61
C-130	flight RF03 (block 61); best AATS, 0152:48 UTC (36.28°N, 132.95°E), elevation 54 m, Oki
Twin Otter	flight RF03 (block 61) (36.497°N, 133.33°E), elevation 41.93 m, Sea of Japan
R/V *Ron Brown*	day 94 (block 66) (30.66°N, 131.50°E), Philippine Sea
Amami surface station	(block 68) (28.44°N, 129.70°E)
	13 April 2001, Oki Island
MISR	orbit 7015, path 111, 0208:14 UTC at block 62
C-130	flight RF08 (block 62); best AATS, 0159:24 UTC (35.78°N, 132.58°E), elevation 45 m
Twin Otter	flight RF08 (block 65) (32.37°N, 132.59°E), elevation 41.12 m
R/V *Ron Brown*	day 103 (block 62) (35.74°N, 132.50°E)
	16 April 2001, Gosan Station, Jeju Island
MISR	orbit 7059, path 116, 0216:37 UTC at block 64
Twin Otter	flight RF10 (block 64) (32.85°N, 127.14°E), elevation 41.92 m, in local mode area
R/V *Ron Brown*	day 106 (block 65) (31.20°N, 126.31°E), in MISR swath, south of local mode
Gosan surface station	(block 64) (33.28°N, 126.17°E)
	27 April 2001, Oki and Amami Islands
MISR	orbit 7219, path 113, 0220:47 UTC at block 63
C-130	flight RF15 (block 63), circuit across southern Korea and back through the Sea of Japan, coincident data taken best AATS: 0236:40 UTC (34.00°N, 130.30°E), elevation 52 m
Twin Otter	flight RF17 (block 63); best AATS, 0221:30 UTC (34.03°N, 129.49°E), elevation 165m
Amami Surface Station	(block 68) (28.44°N, 129.70°E)
	2 May 2001, Gosan Station, Jeju Island
MISR	orbit 7292, path 116, 0239:30 UTC at block 64
C-130	flight RF18 (block 64); best AATS, 0236:00 UTC (33.08°N, 125.38°E), elevation 39 m
Gosan surface station	(block 64) (33.28°N, 126.17°E)

[a]Times are rounded to the nearest minute, and locations are rounded to the nearest hundredth of a degree. The MISR overpass lasts 7.5 min, because a given east-west line of real estate comes into view for each of the nine push broom cameras, successively, over this period, beginning with the 70° forward view. The nominal time given is the midpoint of the sequence over the primary target. "Best AATS" positions are reported in some cases, since this instrument had a short integration time. MISR times report when the nadir camera reached the MISR block indicated.

covered twice in this data set, though it is always more than a few hundred kilometers from any other platform. Figure 1 illustrates with MISR images the locations of the key ACE-Asia platforms at overflight time for each event.

[6] These cases capture a range of clean, polluted, and dusty aerosol conditions, and represent a rich data set for many applications. Regarding MISR validation, they allow us to critically test key assumptions made in the aerosol retrievals about particle and ocean surface properties [*Martonchik et al.*, 1998; *Kahn et al.*, 2001a, 2001b] and to improve the algorithms on the basis of the results. We can then assess the sensitivity of the upgraded retrievals to the range of environmental factors measured in the field.

[7] In this paper, we take a critical initial step by assembling from the multiplatform data snapshots of atmospheric and surface conditions, that amount to optical models and associated uncertainties at selected locations during these five events. Section 2 gives brief descriptions of the instruments and measurement techniques involved, along with references to more detailed discussions of each. In section 3, we present the best accounting we can of the environment in the five cases. We discuss intercomparisons among field measurements at the level of detail appropriate to validating satellite retrievals, point out any discrepancies, and suggest what assumptions or additional data might help resolve them. Some key aspects of the detailed measurement and uncertainty discussions from sections 2 and 3 are summarized in Tables 2 and 3, respectively. In section 4 we produce synthesis optical models for each aerosol layer for each event. In the final section, we summarize the results, and discuss their implications.

2. Measurement Overview

[8] More than 40 instruments contributed to this study (Table 2). They were distributed among six platforms: the Terra satellite, the C-130 and Twin Otter aircraft, the research vessel *Ronald H. Brown*, and the Gosan and Amami surface stations. This section offers brief descriptions of the key instruments aboard each platform, highlighting the important points needed to intercompare results. Detailed discussion of the instruments and measurement techniques, as well as more extensive summaries of their results during the ACE-Asia campaign, are given in the references. In this and subsequent sections, the following abbreviations and symbols are used: RH for relative humidity, AOT for aerosol optical thickness, AOT_{col} to explicitly indicate total column AOT, σ_{ep} for extinction coefficient, σ_{sp} for total scattering coefficient, σ_{bsp} for hemispheric backscattering coefficient, b for hemispheric backscatter fraction ($=\sigma_{bsp}/\sigma_{sp}$), σ_{ap} for absorption coefficient, SSA for single-scattering albedo ($=\sigma_{sp}/\sigma_{ep}$), β_p for 180° backscatter coefficient (used to interpret lidar measurements), and S_a for extinction-to-180°-backscatter ratio ($=\sigma_{ep}/\beta_p$). Ångström exponent is calculated from two wavelengths as

$$A_{xp}(\lambda_1, \lambda_2) = \frac{-\ln[\sigma_{xp}(\lambda_1)/\sigma_{xp}(\lambda_2)]}{\ln[\lambda_1/\lambda_2]}, \quad (1)$$

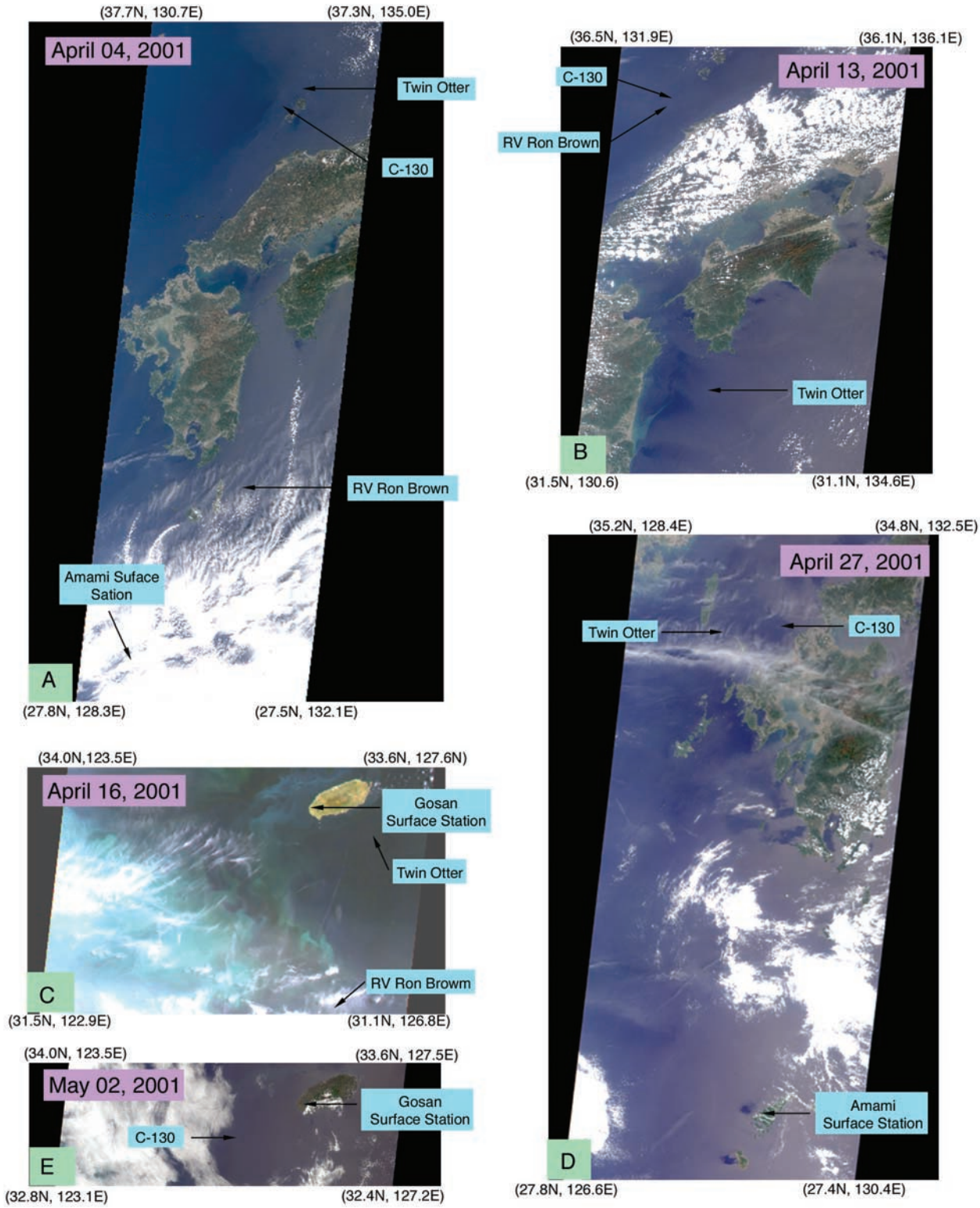

Figure 1. MISR true-color images for the five overpass events, with the locations of the ACE-Asia study platforms indicated: (a) 4 April 2001, Terra orbit 6884, path 112, MISR blocks 61–68, nadir view; (b) 13 April 2001, Terra orbit 7015, path 111, MISR blocks 62–65, 26° aft view; (c) 16 April 2001, Terra orbit 7059, path 116, MISR blocks 64–65, 26° aft view; (d) 27 April 2001, Terra orbit 7219, path 113, MISR blocks 63–68, nadir view; and (e) 2 May 2001, Terra orbit 7292, path 116, MISR block 64, nadir view.

Table 2. Measurements Included in This Study

Acronym	Name	Institution[a]	Measured/Derived Quantities
		Terra Satellite	
MISR	Multiangle Imaging Spectroradiometer	Jet Propulsion Laboratory	top-of-atmosphere reflectance at 9 view angles × 4 wavelengths (446, 558, 672, 867 nm) for a 400-km swath, of 0.275–1.1-km pixels; interpreted as column aerosol optical depth and particle type
		C-130	
Neph-130	integrating nephelometers (five)	University of Washington, Seattle	σ_{sp}, b, $A_{sp}(550,700)$, for all particles and for submicron particles at 450, 550, and 700 nm, at <45% RH; and for 540 nm also at 85% RH, plus β_p at 532 nm and <45% RH; all with about 30-s sampling
PSAP-130	particle soot absorption photometers (two)	University of Washington, Seattle	σ_{ap} at 550 nm and <45% RH, for all particles and for submicron particles; combined with Neph-130 to give SSA
OPC-130	optical particle counter	University of Hawaii	particle size distribution from 120 nm to 15 μm, every 30 s on ascent and descent; 30 s each on unheated, 150°C, 300°C for level legs
APS-130	aerosol particle spectrometer	University of Hawaii	particle size distribution from 0.8 to 12 μm, every 30 s
Chem-130	aerosol particle samplers (three)	University of Hawaii	OC and EC from PC-BOSS sampler, bulk inorganic chemical composition from TAS, and composition for supermicron and submicron size ranges from MOI
SEM/TEM	scanning and transmission electron microscopes	Arizona State University	inorganic particle composition, size, and shape, along with fine-scale structure and mixing states for particles down to 10 nm
AATS-6	Ames Airborne Tracking Sunphotometer	NASA Ames Research Center	AOT at five wavelengths from 380 to 1021 nm, A_{ep}, water vapor extinction, and water vapor density profiles, about every 4 s
		Twin Otter	
AATS-14	Ames Airborne Tracking Sunphotometer	NASA Ames Research Center	AOT at 13 wavelengths from 354 to 1558 nm, A_{ep}, water vapor extinction, and water vapor density profiles, about every 4 s
DMA-TO	differential mobility analyzers (two)	California Institute of Technology	size distribution from 15-nm to 1-μm diameter every 100 s, at dry and ambient RH
APS-TO	aerodynamic particle sizer	California Institute of Technology	size distribution from 0.5 to 20 μm in aerodynamic diameter at ambient RH every 20 s
		R/V Ron Brown	
Mtps-RB	Microtops Sun photometer	NOAA PMEL	AOT at 380, 440, 500, 675, and 870 nm
CPC-RB	condensation particle counter	NOAA PMEL and University of Washington	total particle number concentration for particles having diameters >3 nm, every minute
DMPS-RB	differential mobility particle sizer	NOAA PMEL and University of Washington	aerosol size distribution in 27 bins between 22- and 900-nm diameter, every 15 min
APS-RB	aerodynamic particle sizer	NOAA PMEL and University of Washington	aerosol size distribution between 0.6- and 9.6-μm aerodynamic diameter, every 15 min
Neph-RB	integrating nephelometer	NOAA PMEL	σ_{sp} at 450, 550, and 700 nm and 55% RH, every minute
PSAP-RB	particle soot absorption photometer	NOAA PMEL	σ_{ap} at 565 nm and 55% RH, every minute
Chem-RB	aerosol particle sampler	NOAA PMEL	submicron and supermicron aerosol component mass fractions; dust, sea salt, nss-Ca, nss-Mg, EC, organic matter (POM), H_2O, NH_4, NO_3
NephRH-RB	scanning RH integrating nephelometers	University of Illinois	σ_{sp} and σ_{bsp} at 450, 550, and 700 nm, for particle diameters <10 μm and <1 μm (alternating), scanning 35% < RH < 85%; one sample per hour
MPL-RB	micropulse lidar	NASA GSFC	vertical structure of aerosol and cloud from one-channel (523 nm) backscatter, at 1-min time and 75-m height resolution
SIMBAD	handheld SIMBAD radiometer	Scripps Institution of Oceanography	AOT at 443, 490, 560, 670, and 870 nm and diffuse marine reflectance at 443, 490, 560, and 670 nm
		Gosan Station	
AERONET	CIMEL Sun photometer	NASA GSFC	AOT at 340, 380, 440, 500, 670, 870, and 1020 nm, every 15 min; hourly particle size distribution, phase function, and SSA
MPL-Gos	micropulse lidar	Seoul National University	vertical structure of aerosol and cloud from one-channel (523 nm) backscatter, at 10-min time and 30-m height resolution
DMA-Gos	differential mobility analyzer	Brookhaven National Laboratory	dry size distribution from 0.005- to 0.6-μm diameter once per minute

Table 2. (continued)

Acronym	Name	Institution[a]	Measured/Derived Quantities
OPC-Gos	optical particle counters (two)	KMA/METRI and NOAA/UCSC/BNL	dry particle size distribution from 0.3 to 25 μm diameter every 10 min
HTDMA-Gos	humidified tandem differential mobility analyzer	Brookhaven National Laboratory	size-resolved hygroscopic growth for dry particle diameters between 0.02 and 0.3 μm at controlled RH values, integrated over a few hours on each of 8 separate days
AMS-Gos	Aerodyne mass spectrometer	UMIST	30-min time series averaged loadings, and chemical size distributions of sulfate, nitrate, and organic components for particles in the diameter range 0.03–2.0 μm
Sun-Gos	Sun photometer	KMA/METRI	AOT at 368, 500, 675, 778, and 862 nm, once per minute
Met-Gos	meteorology station	Korea Meteorological Administration	temperature, relative humidity, wind, and atmospheric pressure at 10-m elevation, once per minute
Sunphot-Gos	Carter-Scott Sun photometers (two)	CMDL	AOT at 368, 410, 500, 610, 675, and 862 nm, every minute
Neph-Gos	TSI nephelometers (two)	CMDL	σ_{sp} at 450, 550, and 700 nm as a function of scattering angle and RH, for submicron and sub-10-μm particles, every minute
PSAP-Gos	particle soot absorption photometer	CMDL	σ_{ap} at 565 nm; combined with Neph, single SSA for submicron and sub-10-μm particles, every minute
		Amami Station	
Ceil-Am	ceilometer	Tokyo University of Mercantile Marine	cloud base heights and backscattering profile by aerosol and cloud at 905 nm up to 7.5 km with 15-s time and 15-m height resolutions
Lidar-Am	NIE compact Mie lidar	NIES	backscattering profile (532 nm, 1064 nm) and depolarization ratio profile (532 nm) at 10-s time and 30-m height resolution
PSR-Am	Sun photo-polarimeter	Kinki University	AOT at 443, 490, 565, 670, 765, and 865 nm every minute

[a]PMEL, Pacific Marine Environmental Laboratory; KMA/METRI, Korean Meteorological Administration Meteorological Research Institute; UCSC, University of California, Santa Cruz; UMIST, University of Manchester Institute of Science and Technology.

where the subscript "xp" may be "ep" if extinction or "sp" if scattering coefficients are used. When a single λ is given, A_{xp} was evaluated as the slope of a least squares fit to available data at multiple wavelengths. Similarly, the hygroscopic growth factor, which describes how particle cross section changes with RH, is given as

$$f_{xp}(RH_1, RH_2) = \frac{\sigma_{xp}(RH_1)}{\sigma_{xp}(RH_2)}, \tag{2}$$

where "xp" may be "sp" or "bsp" if total or backscattering coefficients are used, RH_1 is an elevated RH (typically ambient), and RH_2 is a dry reference RH. The relevant wavelengths are either given in Table 2 or are indicated in parentheses after the symbol, in nm. Extinction, absorption, or scattering coefficients are usually reported in Mm^{-1} (inverse megameters); when integrated over the path length, these produce extinction, absorption, and scattering optical depth, respectively. OC is used for organic carbon, EC for elemental carbon, and nss-sulfate for non-sea-salt sulfate. DMA represents differential mobility analyzer, APS is aerodynamic particle sizer, OPC is optical particle counter, PSAP is Particle Soot Absorption Photometer, IPA is individual particle analysis, LTI is low-turbulence inlet, AATS is Ames Airborne Tracking Sunphotometer, and MPL is micropulse lidar. The compass points are abbreviated in the standard way (N, NNE, NE, ENE, etc.). Unless indicated otherwise, component particle sizes are parameterized as area-weighted, lognormal distributions:

$$dN_a(D)/d\log_{10}(D) = \frac{1}{C}\exp\left[-\frac{\log_{10}^2\left(\frac{D}{D_c}\right)}{2\log_{10}^2\sigma}\right], \tag{3}$$

where

$$N_a(D) = \int_{D_1}^{D} \pi D'^2 n(D') dD',$$

$n(D)$ is the number of particles per unit volume at diameter D, D_c is the characteristic diameter of the distribution, σ is the distribution characteristic width, and C is a normalization constant, obtained so the integral of $dN_a(D)$ from D_1 to D_2, the lower and upper limits of the size distribution considered, equals one. When the size range is evaluated from zero to infinity, $C = \sqrt{2\pi}\log_{10}\sigma$, though some measurements are interpreted using this normalization as an approximation to a measured aerosol size range that is narrower.

2.1. MISR Aboard the Terra Satellite

[9] MISR produces 36 simultaneous views of Earth, in a combination of nine angles varying from +70°, through nadir, to −70° in the along-track direction, in four spectral bands [*Diner et al.*, 1998]. It takes 7 min for all nine MISR cameras to view a fixed line on the surface, which sets the effective temporal resolution for coincident observations. At midlatitudes, a given location is imaged about once per week in global mode, providing 275-m resolution data in all four nadir channels, and in the red channels of the other

Table 3. Aerosol and Surface Property Constraints for Key Multiplatform Cases[a]

	Date				
	4 April	13 April	16 April	27 April	2 May
Site, platform	Oki, C-130/TO	Oki, C-130/RB	Gosan, TO	Oki, C-130/TO	Gosan, C-130
Thumbnail description	calm surface, low AOT, low AOT variability	high wind, modest AOT, low AOT variability, some dust, near-surface sea salt	calm surface, low AOT	calm surface, modest AOT, BL pollution, dust aloft, AOT variable, scattered cirrus	calm surface, modest AOT, mainly BL pollution, scattered cloud at BL top
Surface winds, m s^{-1}	3–4	8–10	3–4	1–2	3–5
Surface diffuse reflectivity	0.007 (550), <0.001 (670)	~0.0085 (550), ~0.0024 (670) (includes whitecaps)	~0.009 (550), ~0.0016 (670)	0.007 (550), <0.001 (670) (best guess)	~0.009 (550), ~0.0016 (670) (best guess)
Column aerosol AOT[b]	0.245 ± 0.017 (380), 0.200 ± 0.015 (446), 0.154 ± 0.014 (550), 0.152 ± 0.014 (558), 0.121 ± 0.013 (672), 0.090 ± 0.012 (866), 0.075 ± 0.012 (1021)	0.358 ± 0.025 (380), 0.304 ± 0.024 (446), 0.247 ± 0.024 (550), 0.243 ± 0.024 (558), 0.202 ± 0.023 (672), 0.156 ± 0.023 (866), 0.132 ± 0.023 (1021)	0.143 ± 0.011 (380), 0.116 ± 0.008 (446), 0.090 ± 0.006 (550), 0.089 ± 0.006 (558), 0.073 ± 0.005 (672), 0.057 ± 0.004 (866), 0.050 ± 0.004 (1021)	0.699 ± 0.027 (380), 0.598 ± 0.026 (446), 0.486 ± 0.026 (550), 0.479 ± 0.026 (558), 0.399 ± 0.025 (672), 0.311 ± 0.025 (866), 0.264 ± 0.024 (1021)	0.595 ± 0.026 (380), 0.468 ± 0.026 (446), 0.341 ± 0.025 (550), 0.334 ± 0.025 (558), 0.252 ± 0.025 (672), 0.172 ± 0.024 (866), 0.134 ± 0.024 (1021)
Submicron fraction $AOT_{ep}(550)$[c]	0.80 ± 0.04	0.69 ± 0.05	–	0.66 ± 0.05	0.83 ± 0.05
$A_{ep}(380,1020)$	1.20	1.01	1.07	0.98	1.51
SSA(550)[c]	0.94 ± 0.02	0.93 ± 0.02	–	0.93 ± 0.02	0.94 ± 0.02
Layer 1					
Extent, km	0.075–2.0	0.074–1.2	0.042–1.0	0.106–1.8	0.044–1.3
Layer 1 AOT_{ep}	0.147 ± 0.026 (380), 0.115 ± 0.023 (446), 0.084 ± 0.019 (550), 0.083 ± 0.019 (558), 0.063 ± 0.017 (672), 0.045 ± 0.017 (866), 0.036 ± 0.013 (1021)	0.186 ± 0.018 (380), 0.164 ± 0.017 (446), 0.139 ± 0.017 (550), 0.138 ± 0.017 (558), 0.119 ± 0.017 (672), 0.098 ± 0.016 (866), 0.086 ± 0.016 (1021)	0.047 ± 0.001 (380), 0.037 ± 0.001 (446), 0.028 ± 0.001 (550), 0.027 ± 0.001 (558), 0.022 ± 0.001 (672), 0.017 ± 0.001 (866), 0.015 ± 0.000 (1021)	0.486 ± 0.022 (380), 0.368 ± 0.021 (446), 0.255 ± 0.020 (550), 0.248 ± 0.020 (558), 0.179 ± 0.019 (672), 0.115 ± 0.017 (866), 0.086 ± 0.016 (1021)	0.494 ± 0.082 (380), 0.384 ± 0.069 (446), 0.276 ± 0.055 (550), 0.270 ± 0.054 (558), 0.202 ± 0.044 (672), 0.136 ± 0.033 (866), 0.105 ± 0.028 (1021)
AOT(550) Neph-130	0.079 ± 0.012	0.155 ± 0.026	–	0.335 ± 0.043	0.254 ± 0.054
Submicron fraction $AOT_{ep}(550)$	0.77 ± 0.05	0.57 ± 0.07	0.60	0.65±0.05	0.85 ± 0.04
$A_{ep}(380,1020)$	1.43	0.78	1.13	1.75	1.57
SSA(550)	0.91 ± 0.02	0.92 ± 0.02	0.90	0.92 ± 0.02	0.93 ± 0.02
SSA(550) submicron	not measured	0.87 ± 0.03	0.85	0.91 ± 0.02	0.93 ± 0.02
RH_{ave}	43%	55%	57%	41%	74%
RH_{max}	70%	75%	–	86%	88%
Water fraction $AOT_{ep}(550)$	0.15 ± 0.10	0.16 ± 0.11	–	0.09 ± 0.05	0.32 ± 0.26
Layer 2					
Extent, km	2.0–3.75	1.2–2.1	1.0–2.54	1.8–6.94	1.3–2.3
Layer 2 AOT_{ep}	0.026 ± 0.009 (380), 0.023 ± 0.009 (446), 0.020 ± 0.009 (550), 0.020 ± 0.009 (558), 0.018 ± 0.009 (672), 0.016 ± 0.008 (866), 0.014 ± 0.008 (1021)	0.063 ± 0.018 (380), 0.052 ± 0.017 (446), 0.041 ± 0.017 (550), 0.040 ± 0.017 (558), 0.033 ± 0.017 (672), 0.024 ± 0.016 (866), 0.020 ± 0.016 (1021)	0.020 ± 0.002 (380), 0.012 ± 0.002 (446), 0.006 ± 0.001 (550), 0.006 ± 0.001 (558), 0.004 ± 0.001 (672), 0.002 ± 0.001 (866), 0.002 ± 0.001 (1021)	0.109 ± 0.114 (380), 0.111 ± 0.094 (446), 0.114 ± 0.073 (550), 0.114 ± 0.072 (558), 0.116 ± 0.057 (672), 0.119 ± 0.042 (866), 0.121 ± 0.034 (1021)	0.022 ± 0.026 (380), 0.018 ± 0.025 (446), 0.014 ± 0.023 (550), 0.014 ± 0.023 (558), 0.011 ± 0.021 (672), 0.009 ± 0.019 (866), 0.007 ± 0.018 (1021)
AOT(550) Neph-130	0.019 ± 0.002	0.044 ± 0.005	–	0.076 ± 0.011	0.020 ± 0.004
Submicron fraction $AOT_{ep}(550)$	0.49 ± 0.06	0.70 ± 0.05	0.85	0.28 ± 0.04	0.65 ± 0.09
$A_{ep}(380,1020)$	0.62	1.14	2.53	−0.11	1.12

Table 3. (continued)

	Date				
	4 April	13 April	16 April	27 April	2 May
SSA(550)	0.95 ± 0.01	0.91 ± 0.02	–	0.94 ± 0.01	0.95 ± 0.01
SSA(550) submicron	not measured	0.89 ± 0.02	–	0.85 ± 0.03	0.94 ± 0.02
RH_{ave}	14%	32%	5.6%	9%	74%
RH_{max}	39%	28%	7.0%	37%	100% (cloud)
Water fraction $AOT_{ep}(550)$	0.05 ± 0.02	0.11 ± 0.06	–	0.02 ± 0.01	0.39 ± 0.29
			Layer 3		
Extent, km	–	–	–	–	2.3–5.48
Layer 3 AOT_{ep}	–	–	–	–	0.037 ± 0.025 (380), 0.032 ± 0.025 (446), 0.026 ± 0.024 (550), 0.026 ± 0.024 (558), 0.021 ± 0.024 (672), 0.017 ± 0.023 (866), 0.014 ± 0.023 (1021)
AOT(550) Neph-130	–	–	–	–	0.017 ± 0.002
Submicron fraction $AOT_{ep}(550)$	–	–	–	–	0.63 ± 0.05
$A_{ep}(380,1020)$	–	–	–	–	1.69
SSA(550)		–	–	–	0.92 ± 0.01
SSA(550) submicron	–	–	–	–	0.89 ± 0.02
RH_{ave}	–	–	–	–	9%
RH_{max}	–	–	–	–	59%
Water fraction $AOT_{ep}(550)$	–	–	–	–	0.03 ± 0.02
			Above the Top Layer Sampled[c]		
AOT_{ep}	0.072 ± 0.016 (380), 0.061 ± 0.015 (446), 0.049 ± 0.014 (550), 0.048 ± 0.013 (558), 0.039 ± 0.013 (672), 0.029 ± 0.012 (866), 0.024 ± 0.012 (1021)	0.110 ± 0.025 (380), 0.087 ± 0.024 (446), 0.065 ± 0.024 (550), 0.063 ± 0.024 (558), 0.049 ± 0.024 (672), 0.034 ± 0.023 (866), 0.027 ± 0.023 (1021)	0.079 ± 0.010 (380), 0.067 ± 0.007 (446), 0.055 ± 0.005 (550), 0.054 ± 0.005 (558), 0.046 ± 0.003 (672), 0.037 ± 0.003 (866), 0.033 ± 0.002 (1021)	0.130 ± 0.026 (380), 0.115 ± 0.026 (446), 0.097 ± 0.026 (550), 0.096 ± 0.026 (558), 0.083 ± 0.025 (672), 0.068 ± 0.025 (866), 0.060 ± 0.024 (1021)	0.037 ± 0.025 (380), 0.032 ± 0.025 (446), 0.026 ± 0.024 (550), 0.026 ± 0.024 (558), 0.021 ± 0.024 (672), 0.017 ± 0.023 (866), 0.014 ± 0.023 (1021)
$A_{ep}(380,1020)$	1.10	1.44	0.89	0.79	0.95

[a]Entries in this table are best estimate values under ambient conditions. SSA values are hydrated to ambient RH, using growth factors determined from hydrated nephelometers (Table 2); see text for further details. The following abbreviations are used: TO, Twin Otter; RB, research vessel *Ron Brown*. Wavelength (in nanometers) is given in parentheses where needed. Water fraction $AOT_{ep}(550)$ is the difference between AOT at ambient RH and at 30% RH, as deduced from Neph-130. The multispectral AOT numbers reported are as follows: 4 April, the average of AATS-6 on the C-130 and AATS-14 on the TO; 13 April, 27 April, and 2 May, AATS-6 only; 16 April, AATS-14 only. Because of highly variable cirrus on 27 April, the AATS-6 observations for layer 1 were obtained from the profile that began at 0236 UTC, those for layer 2 were obtained from the 0103 UTC profile, and the above-the-top-layer observations were obtained from the transit profile at 0313 UTC. For all other cases, the profiles used are the same as those in the corresponding profile plots.

[b]Uncertainties given for Neph-130 + PSAP-130 observations are the formal measurement error [*Anderson et al.*, 2003b]. Additional uncertainty arises because of ambient variation, as discussed in the text. For the total-column AATS data, these are assessed on the basis of short-distance horizontal variability and combined as the root-sum-square with the formal measurement error, which amounts to assuming that the two contributions are independent. For the AATS-14 layer AOT, only the horizontal variability term is retained, since formal measurement errors should cancel between layer top and bottom. For AATS-6 layer data, horizontal variability and half the formal measurement error are combined, to account for pointing uncertainty with that instrument [see *Redemann et al.*, 2004].

[c]For the above-the-top layer, we assume the unmeasured SSA(550) = 0.98 and submicron fraction $AOT_{ep}(550)$ = 0.98, as additional constraints to produce total-column quantities.

eight cameras. The remaining 24 channels of data are averaged on board the spacecraft to 1.1-km resolution. For each MISR event day during ACE-Asia, we also designated a MISR local mode site, 300-km along-track and 400-km cross-track, over which data were acquired at 275-m resolution in all 36 channels.

[10] Prelaunch theoretical studies indicated that MISR spectral radiances, measured at precisely known air mass factors ranging from 1 to 3, could provide tight constraints on AOT_{col} over land and water. Along with the wide range of scattering angles sampled (about 50°–160° at midlatitudes), MISR would offer constraints on particle shape, size distribution, and composition, particularly over dark, uniform ocean surfaces [*Kahn et al.*, 2001a, 1998; *Martonchik et al.*, 1998]. If these expectations are met, global maps of aerosol amount and of aerosol air mass type (in about a dozen broad classes) can be derived routinely from MISR data.

2.2. Nephelometers Aboard the C-130

[11] A suite of instruments operating downstream of the LTI on the C-130 [*Lafleur*, 1998] measured aerosol visible light scattering and absorbing properties [*Anderson et al.*, 2003a, 2003b]. The σ_{sp} and σ_{bsp} were measured at three wavelengths, using two integrating nephelometers (model 3563, TSI, Inc., St. Paul, Minnesota); one measured total sampled aerosol while the second measured only submicron particles (defined as aerodynamic diameter less than 1 μm at low RH). Both operated at RH < 45%. To provide information on aerosol hygroscopicity, a second pair of single-wavelength nephelometers (model M903, Radiance Research, Seattle, Washington) operated at low (<45%) and high (85%) RH, respectively, yielding the dependence of scattering on RH, assuming the dependence is exponential in form [*Kasten*, 1969]. The σ_{ap} was measured for both total and submicron aerosol, at low RH and 550-nm wavelength, with a pair of differential transmission absorption photometers (model PSAP, Radiance Research, Seattle, Washington), and β_p at low RH was measured with a modified TSI nephelometer [*Doherty et al.*, 1999]. This combination of measurements permits the following quantities to be derived: (1) σ_{ep} at ambient RH (which generally compares well with an independent measurement by differential Sun photometry [*Redemann et al.*, 2003]), (2) the scattering, backscattering, and absorption components of extinction, (3) the submicron and supermicron particle contributions to the components of extinction, and (4) basic optical properties: SSA, b, S_a, and A_{sp}. Neph-130 and PSAP-130 data were calibrated and corrected for instrumental nonidealities according to established recommendations [*Anderson and Ogren*, 1998; *Bond et al.*, 1999]. Uncertainties associated with noise, calibration, correction factors, and RH adjustments were used to determine 95% confidence values for each reported quantity.

2.3. OPC, APS, and Chemical Samplers Aboard the C-130

[12] Two instruments aboard the C-130 measured particle size distributions over optically active diameter ranges during flight. An OPC (modified LAS-X ASASP) detected particles from 120 nm to 15 μm, and an APS (TSI model 3020) recorded 0.8–12-μm particles. Both drew air from the same LTI as the nephelometers. During level flight, sample air to the OPC was periodically diverted through heated tubes to give some indication of particle chemical composition [*Clarke*, 1991]. The APS ran in correlated mode to minimize the influence of "ghost particles" caused by recirculation within the sensing volume. It operated at the same RH as the aerosol inlet, lower than ambient. OPC samples were dried further by mixing with filtered and desiccated air. The OPC, calibrated with spheres of known refractive index, provides optically effective sizes (OES) for all particle shapes and compositions. Optical properties can be calculated directly from OES for particles having refractive indices near the calibration value (e.g., Asian dust); for wet and absorbing aerosols, corrections for refractive index differences are made on the basis of measured composition. This approach is more easily justified for the OPC than the APS, but the resulting dry SSA values are in agreement with those from Neph-130 + PSAP-130 (section 2.2), providing a good overall check. Estimated uncertainties in derived ambient extinction are about 15% [*Clarke et al.*, 2002]; additional uncertainties are introduced when converting OES to mass equivalent size, a step not needed for the optical models developed in section 4.

[13] Aerosol chemical composition was measured with three samplers. OC and EC were collected on quartz filters in a PC-BOSS sampler designed to minimize positive and negative vapor artifacts. The filters were analyzed using a Sunset Labs thermal/optical instrument and the NIOSH technique [*Huebert et al.*, 2004]. Bulk inorganic chemical composition was measured [*Kline et al.*, 2004] by collecting aerosols in a total aerosol sampler (TAS) mounted outside the fuselage. It used a replaceable diffuser liner cone and Teflon filter to collect every particle that enters its tip, to be extracted for ion chromatography analysis. By sampling isokinetically, TAS avoids any inlet or plumbing artifacts, even for large dust particles. The third sampler is an eight-position multiple-micro-orifice cascade impactor (MOI) made by MSP Corporation, which received air from a dedicated low-turbulence inlet. Its aluminum substrates and backup filters were also analyzed by ion chromatography.

[14] For the current study, these data were interpreted as follows: Coarse-mode particles are partitioned between dust and sea salt, on the basis of the calcium to sodium ion abundance ratio. Sea-salt index of refraction and hygroscopicity are obtained from simultaneous levitated drop experiments [*Tang and Munkelwitz*, 1991], whereas dust is assumed to have index of refraction 1.58-0.0006i and to be nonhygroscopic. Reducing the poorly constrained real part of the dust index of refraction to 1.53 or 1.51 (*Clarke et al.* [2004] and Table 5) affects the resulting size distributions about 2%, well below the overall experiment uncertainty. The submicron particles are assumed to be homogeneous spheres, a mix of four components: sulfate and OC comprising the volatile fraction, and for the refractory component, EC and dust or fly ash, with the added constraint that the volume distribution of dust should diminish for decreasing particle size. The hygroscopicity of the volatile fraction is taken as equal to that derived for the pollution component in the INDOEX and ACE-2 experiments [*Clarke et al.*, 2002]. Many of

these assumptions will be relaxed in future analyses of the ACE-Asia data.

2.4. IPA Samples Taken Aboard the C-130 and *Ronald H. Brown*

[15] Aerosol samples for individual particle analysis by scanning electron microscope (SEM) and transmission electron microscope (TEM) were collected with filter and microimpactor systems connected to the low-turbulence inlet on the C-130. SEM samples were collected with two Programmable Streaker Samplers (PIXE International) configured for one-stage filtration on polycarbonate membranes. TEM samples were collected on 3-mm grids with a three-stage microimpactor (California Measurements). One or more sample sets was collected on each level leg of flight. SEM and TEM samples were also continuously collected using Streakers on the *Ron Brown*; sample duration was 2 hours.

[16] Inorganic particle composition, size, and shape are measured with an automated *S*EM [*Anderson et al.*, 1996]. Minimum particle size is about 100 nm. Black carbon particles are examined manually with a field emission SEM; minimum particle size is about 10 nm. TEM is used to examine fine-scale structure and mixing states of particles as small as 10 nm. The TEM also allows analysis of nitrates that survive in high vacuum. However, low collection efficiency limits the examination of particles smaller than 50 nm.

2.5. AATS Instruments Aboard the C-130 and Twin Otter

[17] The 6-channel NASA Ames AATS-6 operated on 15 of the 19 research flights of the C-130; its 14-channel counterpart, AATS-14, flew successfully on 19 research flights of the Twin Otter. AATS-6 and AATS-14 measure direct solar beam transmission in 6 and 14 wavelength channels (380 to 1021 and 354 to 1558 nm, respectively). In both AATS instruments, azimuth and elevation motors controlled by differential Sun sensors rotate a tracking head so as to lock on to the solar beam and keep detectors normal to it. The tracking head of each instrument mounts external to the aircraft skin, to minimize blockage by aircraft structures and also to avoid data contamination by aircraft window effects. Each channel consists of a baffled entrance path, interference filter, photodiode detector, and preamplifier, which are temperature-controlled to avoid thermally induced calibration changes. The data yield AOT spectra and column water vapor. Vertical differentiation of these data, taken during suitable flight patterns, yields extinction spectra and water vapor concentration. Examples are given by *Russell et al.* [1999], *Schmid et al.* [2000, 2003a, 2003b], *Livingston et al.* [2003], and *Redemann et al.* [2004]. AATS AOT is reported in this paper at wavelengths common to other instruments by interpolating along linear (for AATS-6) or quadratic (for AATS-14) fits to log (AOT_{ep}) versus log (λ). $A_{ep}(\lambda)$ is derived as the slope of the line in log (EXTINCTION) versus log (λ) space, passing through EXTINCTION(380) and EXTINCTION(1020).

[18] Premission and postmission radiometric calibration for the ACE-Asia field campaign was determined via Langley plots using data taken at the high-altitude Mauna Loa Observatory in March and June of 2001, respectively. For AATS-14, comparison of premission and postmission calibration constants, time interpolation from premission to postmission values, and inspection of high-altitude AOT spectra during the campaign, produce an effective calibration that was less than 0.6% different from premission values in 11 channels and less than 1.5% different in the remaining 3 channels. For AATS-6, the same procedure, in addition to in-flight and ground-based comparisons with AATS-14, reveals that premission calibration constants need to be used for flights until 12 April 2001 (C-130 flight RF07). Thereafter, postmission calibration is applied. Because of occasional poor tracking performance of AATS-6, a tracking uncertainty of 2% is added to the uncertainties in the calibration constants. Methods for AATS data reduction and error analysis are given by *Russell et al.* [1993] and *Schmid et al.* [2003b]. Details that pertain to the analysis of *AATS* data obtained in ACE-Asia are described by *Schmid et al.* [2003a] for AATS-14 and *Redemann et al.* [2004] for AATS-6.

2.6. DMA and APS Aboard the Twin Otter

[19] Aerosol size distributions were measured by DMA systems and APS on board TO during ACE-Asia. Two DMA systems operated in parallel inside the main cabin of the TO [*Wang et al.*, 2003b]. One measured dry aerosol size distribution by passing the aerosol flow through a Nafion drier prior to the measurement; the other operated at ambient RH, using an active RH controller [*Wang et al.*, 2003b]. The size measurement sections of the two systems downstream of the drier and active RH controller were identical. The main components of the measurement section were a cylindrical DMA (TSI Inc., model 3081) and a condensation particle counter (TSI Inc., model 3010) having a 50% counting efficiency at 10 nm. All the flows associated with the DMA were monitored and maintained by feedback controllers to compensate for environmental changes during airborne measurement. Using the scanning mobility technique, each DMA system generates a size distribution from 15-nm to 1-μm diameter every 100 s. The aerosol sample flows for the DMA systems were drawn from the TO community inlet, which was shared by other instruments. For the particle size range measured by the DMA systems, the aerosol transmission efficiency through the community inlet was established as 100%. Data from the DMA systems were analyzed using the data inversion procedure described by *Collins et al.* [2002].

[20] An APS (TSI model 3320), having a measurement range of 0.5 to 20 μm aerodynamic diameter, was mounted under the left wing of the TO. The APS infers particle size by measuring the velocity of particles inertially accelerated in an expanding air stream; large particles undergo smaller acceleration and reach lower velocity than small particles. To derive aerosol size from APS measurements, particle size and density are required; the procedure used is described in detail by *Wang et al.* [2003a]. The overall uncertainties amount to about 5% for DMA size, 10% for APS size, and 10% for DMA and APS particle concentration.

2.7. Sun Photometer and Aerosol In Situ Chemical and Physical Properties Measurements Aboard the *Ronald H. Brown*

2.7.1. AOT

[21] AOT was derived from a five-channel handheld Microtops Sun photometer (Solar Light Co.), having built-

in pressure and temperature sensors, and an associated global positioning system (GPS) [*Quinn et al.*, 2002]. To reduce pointing errors caused by ship motions, the maximum voltage from a 1-min sequence of 10-s measurements was kept. In converting the raw signal voltages to AOT, corrections were applied for Rayleigh scattering, ozone opacity, and the effect of Earth's curvature on air mass. The instrument was calibrated using a Langley plot approach, prior to the cruise and again one year later. Calibration constants in all channels differed less than 0.9% between the two calibrations, representing about 0.01 variation in AOT.

2.7.2. Inlet

[22] Aerosol particles were sampled 18 m above the sea surface through a heated mast designed to maintain isokinetic flow and to minimize supermicron particle losses. The lower 1.5 m of the mast was heated to dry the aerosol to an RH of 55 ± 5%, allowing constant instrumental size cuts through variations in ambient RH. Fifteen 1.9-cm diameter electrically conductive polyethylene or stainless steel sampling tubes extend into this heated zone to direct the air stream at flows of 30 L min^{-1} to the various aerosol sizing/counting instruments and impactors [*Quinn et al.*, 2001; *Bates et al.*, 2001, 2004].

2.7.3. Aerosol Number Size Distributions and Concentrations

[23] Details of the particle number size distributions and concentrations are given by *Bates et al.* [2001]. Briefly, total particle number concentrations were measured with a condensation particle counter (CPC, model 3010, TSI, St. Paul, Minnesota) operated directly off one of the 1.9-cm sampling tubes. The same tube supplied ambient air to a differential mobility particle sizer (DMPS) located inside a humidity-controlled box at the base of the sampling mast. Data were collected in 27 size bins having midpoints ranging from 22- and 900-nm diameter.

[24] Another 1.9 cm tube was connected to an APS (model 3320, TSI) located in the humidity-controlled box measuring the number size distribution between 0.6 and 9.6 μm aerodynamic diameter. The APS data were converted from aerodynamic diameters to geometric diameters at 55% RH using calculated densities and the water masses associated with the inorganic ions at 33% and 55% RH. The densities and associated water masses were calculated with a thermodynamic equilibrium model using the measured chemical data [*Quinn et al.*, 2001], and the combined DMPS and APS number distributions were converted to surface area distributions. The derived number size distributions are uncertain to about ±20%, dominated by instrumental particle sizing errors and counting errors due to flow instabilities.

2.7.4. Aerosol Scattering and Absorption Coefficients

[25] The σ_{sp} was measured with an integrating nephelometer (model 3563, TSI Inc.) at 55% RH, at three wavelengths. Values were corrected for offset [*Anderson and Ogren*, 1998], and for nephelometer angular nonidealities, including truncation errors and non-Lambertian response [*Quinn et al.*, 2001]. For a 30-min averaging time, a quadrature sum of errors yielded absolute uncertainties of 4.1 and 20 Mm^{-1}, corresponding to low and high values of σ_{sp} equal to 24 and 110 Mm^{-1}, respectively. The σ_{ap} was measured at 565 nm and 55% RH by monitoring the change in transmission through a filter with a PSAP (Radiance Research) and reported at 550 nm [*Quinn et al.*, 2001]. A quadrature sum of errors yields absolute uncertainties of 0.38 and 2.8 Mm^{-1} for σ_{ap} equal to 0.68 and 13 Mm^{-1}, respectively, for a 30-min averaging time. Neph-RB and PSAP-RB values are reported at 0°C, 1013 mbar, and 55 ± 5% RH.

[26] Independently, σ_{sp}, σ_{bsp}, and their RH dependence were measured with a scanning nephelometry system (NephRH-RB) [*Carrico et al.*, 2003], using the same particle size limits and wavelengths as Neph-RB. One nephelometer (model 3563, TSI Inc.) operated at "dry" conditions (RH 19 ± 5%), while two downstream nephelometers (model 3563, TSI, Inc. and model M903, Radiance Research, Inc.) operated with controlled RH that scanned between 35% and 85%. Increasing RH scans started from the "dry" aerosol condition and decreasing RH scans started from the "hydrated" aerosol condition to examine the aerosol's deliquescence, crystallization, hysteresis, and metastable properties. Corrections were made for particle loss (∼5%) and nephelometer nonidealities [*Anderson and Ogren*, 1998], and adjusted to 0°C and 1013 mbar. Results at controlled RH values are provided for σ_{sp} and σ_{bsp} as f_{sp}(RH, 19 ± 5%) and as f_{bsp}(RH, 19 ± 5%); results are given for λ = 550 nm and particle diameter <10 μm unless specified otherwise. Comparing σ_{sp} values from the Neph-RB, which only warms the ambient sample an average of 4°C, to σ_{sp} values from the NephRH-RB, gives direct evidence about the state of hydration of the aerosol at ambient conditions. A_{sp}(450,550), b(550), and SSA(550) were also derived, and reported at ambient conditions. σ_{ap} at RH ∼55% from the PSAP-RB were used to calculate SSA.

2.7.5. Mass Fractions of Aerosol Chemical Components

[27] Submicron and supermicron aerosol chemical component mass fractions were calculated from measured chemical component concentrations, and filters weighed before and after sample collection [*Quinn et al.*, 2001]. Mass fraction uncertainties at the 95% confidence level are based on a quadratic sum of chemical concentration uncertainties, along with gravimetrically determined mass. Uncertainties for the inorganic ionic components (nss-$SO^{4=}$, NH^{4+}, sea salt, and NO_3^-) range from ±3% to ±7%. Uncertainties are higher for OC (±25%), EC (±10%), and dust (±20%).

2.8. MPL Aboard the *Ronald H. Brown*

[28] The NASA MPLNet project [*Welton et al.*, 2001] deployed a unit aboard the RB, forward of the vessel's stacks to limit any influence from the ship engine exhaust, and was housed inside a climate-controlled sea container. The instrument is a single-channel, semiautonomous, eye-safe lidar system that yields vertical structure of clouds and aerosols [*Spinhirne et al.*, 1995]. Installation of the MPL and data processing were identical to those described by *Welton et al.* [2002] for the INDOEX 1999 cruise. Raw MPL data, acquired at 1-min time resolution and 75-m vertical resolution, were converted into uncalibrated lidar signals [*Campbell et al.*, 2002; *Welton and Campbell*, 2002]. Aerosol extinction profiles were calculated using the algorithm described by *Welton et al.* [2000], for times coincident with Mtps-RB measurements, to help interpret

backscatter in terms of AOT. In this analysis, the extinction-to-backscatter ratio is assumed constant over the column. The Mtps-RB data were analyzed by the NASA Sensor Intercomparison and Merger for Biological and Interdisciplinary Oceanic Studies (SIMBIOS) project [*Knoblespiesse et al.*, 2003].

2.9. SIMBAD Spectral Water Reflectance and AOT From the *Ronald H. Brown*

[29] Diffuse marine reflectance (i.e., the reflectance of the water body) and AOT were measured from the bow of the RB by a SIMBAD radiometer [*Deschamps et al.*, 2004]. The instrument is portable and does not require the ship to stop. For diffuse marine reflectance, the radiometer is aimed at the ocean surface from the side of the ship lit by the Sun, at an angle of 45° from nadir, and a relative azimuth angle of 135°. With the help of a polarizer, this viewing geometry allows one to reduce substantially, skylight reflected by the surface in the instrument's field of view [*Fougnie et al.*, 1999]. For AOT, the radiometer is aimed at the Sun. The same 2.5° field-of-view optics and the same detectors are used in Sun- and sea-viewing modes, but with different electronic gains. The radiometric data are acquired simultaneously in five spectral bands in each mode. To transform water-leaving radiance into water reflectance, downward solar irradiance at the surface is calculated, which can be done accurately under clear skies or when the Sun's fractional cloud cover is less than 0.2.

[30] The AOT root-sum-square errors, due mostly to calibration uncertainty, are ±0.02, ±0.02, ±0.02, ±0.01, and ±0.01 at 443, 490, 560, 670, and 870 nm, respectively, for an air mass of unity (smaller at higher air mass). The uncertainty in diffuse marine reflectance, due to various factors, especially calibration errors, residual skylight reflection, and polarization of the water body, is $\pm 1.4 \times 10^{-3}$ (6%), $\pm 1.1 \times 10^{-3}$ (6%), $\pm 0.4 \times 10^{-3}$ (8%), and $\pm 0.2 \times 10^{-3}$ (23%) in the four shorter spectral bands, for an ocean containing 0.1 mg m^{-3} of chlorophyll-a. No water reflectance is obtained at 870 nm, where the ocean is assumed black. To insure data quality, the instrument was calibrated in Sun- and sea-viewing modes before and after the experiment using the Bouguer-Langley method and an integrating sphere, and average calibration coefficients were used in the data processing.

2.10. AERONET Sun Photometers at Gosan and Other Surface Stations

[31] AERONET is a collaborative, globally distributed network of identical, seven-channel Sun- and sky-scanning spectral radiometers that retrieve column integrated aerosol parameters including AOT. Data are taken every 15 min (given cloud-free conditions), are processed and calibrated through a common data stream, and exhibit nominal accuracy of ±0.01 [*Eck et al.*, 1999; *Holben et al.*, 1998; *Smirnov et al.*, 2000]. Hourly sky scans are made through the aureole in the almucantar, yielding particle size distribution, phase function, spectral modal AOT, spectral SSA, and spectral complex index of refraction [*Dubovik and King*, 2000]. Accuracy of retrieved parameters varies according to environmental conditions; however, quality-assured data typically yield SSA with ±0.03 absolute accuracy, real index of refraction to ±0.02, and a size distribution range from 0.05 to 15 μm [*Dubovik et al.*, 2000].

[32] Sixteen sites were located within the greater ACE-Asia study area during the campaign, including Beijing, China; Dunhuang, China; IMGRASS (NE China); Noto, Japan; Osaka, Japan; Okinawa, Japan; Shirahama, Japan; Dalanzadgad, Mongolia; Anmyon Island, South Korea; Gosan, South Korea; Lan-Yu Island, Taiwan; Wan-Li, Taiwan; NCU, Taiwan; Midway Islands; Mauna Loa, Hawaii; and Lanai, Hawaii. Data were collected from March to June and posted on the AERONET website http://aeronet.gsfc.nasa.gov. Observations at Gosan began 4 April and continued through 20 June.

2.11. MPL at the Gosan Surface Site

[33] Seoul National University deployed a single-channel MPL (SES Inc., United States) [*Yoon and Won*, 1998; *Murayama et al.*, 2001] at the Gosan surface site. Background information is given by *Spinhirne et al.* [1995] and *Welton et al.* [2000]. The vertical resolution was adjusted to 30 m, and the MPL was set to average and analyze the backscattered signal every 10 min. The σ_{ep} profiles were retrieved from the signals by the method of *Fernald* [1984] and *Klett* [1981]. From these, the altitude and thickness of Asian dust layers, as well as AOT, are derived.

2.12. DMA, OPC, Chemical Size Distribution, and AOT at the Gosan Surface Site

[34] Intensive measurements of aerosol size, concentration, and chemical composition were obtained from a suite of instruments at Gosan. They included two DMAs [*Brechtel et al.*, 1998; *Brechtel and Kreidenweis*, 2000], two OPCs [*Brock et al.*, 2003; *Lee et al.*, 2002], and two mass spectrometers providing aerodynamic particle size distributions [*Zelenyuk and Imre*, 2001], along with Sun photometer and meteorological measurements. All particle number size measurements were conducted at RH < 30% to remove particle-bound water and facilitate instrument intercomparisons. Size-resolved particle growth factor, as a function of RH, was measured by a Humidified Tandem Differential Mobility Analyzer (HTDMA) [*Brechtel and Kreidenweis*, 2000; *Buzorius et al.*, 2002], to help translate dry size distribution to ambient RH. Mobility number size distributions were obtained over the diameter range 0.005–0.6 μm, whereas OPC distributions were observed over the diameter range 0.1–25 μm [*Lee et al.*, 2002]. All number size distribution measurements were corrected for size-dependent inlet losses [*Willeke and Baron*, 1993].

[35] Daily averaged chemical size distributions of sulfate, nitrate, and organic-containing particles from Berner impactors, covered the aerodynamic size range 0.1–10 μm. Size-dependent particle density and refractive indices, calculated from the impactor data, were used to adjust the aerodynamic to mobility size and to correct the OPC data for index-of-refraction effects, respectively. The use of realistic, size-resolved refractive indices significantly altered the OPC diameter and therefore the moments of the OPC size distribution.

[36] A ground-based, five-channel Sun photometer made AOT measurements once per minute. We compare this spectral AOT data with observations from the Gosan AERONET and AATS-6 instruments in section 3. Meteo-

rological measurements, including surface temperature, RH, near-surface wind speed and direction, and atmospheric pressure were sampled once per minute at 10-m elevation.

2.13. AOT, Radiation, and In Situ Aerosol Optical Properties at the Gosan Surface Site

[37] Climate Monitoring and Diagnostics Laboratory (CMDL) made AOT and surface radiation budget observations complementary to the measurements described in section 2.12 [*Dutton et al.*, 1994; *Dutton and Christy*, 1992; *Dutton and Bodhaine*, 2001]. The instrumentation included two Carter-Scott six-channel Sun photometers and broadband solar radiometers for direct, diffuse, total solar irradiance, all mounted on a Sci-Tech active solar tracker atop a 30-m tower. The instruments were calibrated at CMDL facilities in Boulder, Colorado, both before and after the 1-year deployment. The Sun photometers were repeatedly calibrated on site during the field phase. One-minute average data from all radiometers were derived from 1-Hz sampling; Sun photometer sampling was once per minute on the minute. The broadband radiometer calibration accuracy is documented by *Ohmura et al.* [1998], with recent enhancements outlined by *Dutton et al.* [2001]. Accuracy of the spectral AOT is believed to be approximately 0.02 or 5%, whichever is larger. On-site personnel provided minimal field instrument maintenance and cleaning, and the data were collected several times daily and transferred by phone line to Boulder, Colorado, for processing.

[38] In addition, σ_{sp} was measured with two nephelometers (model 3563, TSI, Inc.) at three wavelengths, as a function of scattering angle (7°–170° and <90°) and RH (50–95%). Corrections for noise, instrument drift, calibration and truncation of forward scattered radiation were made according to *Anderson and Ogren* [1998]. The σ_{ap} was measured at 565 nm by a Radiance Research PSAP, with data corrections for sample area, flow rate, and nonidealities in the manufacturer's calibration based on *Bond et al.* [1999]. Aerosol impactors allowed us to determine σ_{sp} and σ_{ap} separately for submicron and sub-10-μm-sized aerosol. Detailed descriptions of this instrumentation, its operation, and associated uncertainties and variability are given by *Sheridan et al.* [2001] and *Delene and Ogren* [2002]. From these measurements we calculate aerosol intensive properties: SSA, $A_{sp}(550,700)$, f(RH), and b.

2.14. Ground-Based Atmospheric Column Measurements at Amami-Oshima Island

[39] A portable, six-channel photopolarimeter, PSR-1000, operated at Amami-Oshima Island. The results were interpreted in terms of spectral AOT and A_{ep}, using an algorithm described by *Sano et al.* [2003]. A Glan-Thompson prism was attached in front of the filters to make polarization measurements for retrieving aerosol refractive index. Langley plot calibration measurements were taken at the summit of Mount Haleakala in Hawaii in February 2001. A second cross-calibration was done in February 2001 at the Shirahama AERONET site in Japan, by direct comparison with a freshly calibrated Cimel CE-318.

[40] Lidar observations were taken at Amami from 2–7 April with a National Institute for Environmental Studies two-channel polarization lidar; from 13–26 April the Tokyo University of Mercantile Marine Vaisala CT25K ceilometer operated. Cloud screening was performed, using a threshold method, on raw 10-Hz lidar data that was averaged and recorded every 3 s. The $\beta_p(532)$ was then derived from the average of all cloud-free profiles in a 15-min period, using a two-component inversion algorithm [*Fernald*, 1984; *Sugimoto et al.*, 2001]. As part of this procedure, S_a was adjusted so the lidar-obtained AOT matched the Sun photometer value obtained between 0630 and 0700 UTC. The cielometer was designed primarily to detect cloud base, and was calibrated by the manufacturer using a known backscattering material. The β_p for free troposphere aerosols, derived from 10-min averaged ceilometer data, are less accurate than those from the lidar because of insufficient sensitivity to aerosols over the mixed layer, comparatively wide bandwidth and low energy, and additional attenuation by water vapor absorption at the ceilometer wavelength. However, the data cover a period when the National Institute for Environmental Studies (NIES) instrument was not operating.

2.15. Regional Meteorology Analysis

[41] Meteorological situations were evaluated using gridded fields from two global models, visible and infared imagery from operational weather satellites, and routine and intensive surface and upper air observations. The NOGAPS model [*Hogan and Rosemond*, 1991] is a global spectral model with a hybrid-sigma vertical coordinate system. The fields used here are at 1° × 1° horizontal resolution, extending from the surface to 150 hPa on isobaric levels, and include the standard thermodynamic and dynamical variables. The vertical resolution in the lower troposphere is high, having eight levels between the surface and 700 hPa (~3 km). The data assimilation/forecast cycle produced analysis fields at 0000 and 1200 UTC each day, and short-term forecast fields at 0600 and 1800 UTC. We also made use of fields from the NCEP/NCAR Reanalysis archive [*Kalnay et al.*, 1996]. The resolution is lower, 2.5° × 2.5°, but analyzed fields are available four times per day, and a much broader selection of thermodynamic and dynamical variables is available. Further, the same model system has been used for the period from 1957 to the present, allowing unbiased assessment of interannual variability. These model results are suitable for diagnostic evaluation of synoptic-scale features, but cloud and precipitation distributions must be estimated using satellite and in situ observations. We also made use of air mass trajectory calculations (HYSPLIT (Hybrid Single-Particle Lagrangian Integrated Trajectory) model, 2002, available at http://www.arl.noaa.gov/read/hysplit4.html, NOAA Air Resources Laboratory, Silver Spring, Maryland). to diagnose the paths of air parcels prior to their arrival in the sampling areas. Further discussion of meteorological influences and transport patterns is given by *Merrill and Kim* [2004].

3. Environmental Snapshots of Five Multiplatform Events

[42] This section presents a synthesis of environmental constraints available for the five occasions when MISR took space-based data coincident with two or more participating

ACE-Asia surface and airborne platforms (Table 1). All MISR observations occurred between 0200 and 0240 UTC. For each event, we review the regional meteorology, air mass history, surface wind, wave, and reflectivity conditions, and available column-integrated as well as layer-by-layer information about spectral AOT and particle microphysical properties. Where similar measurements were taken multiple times in a sampling region, comparisons among these quantities are discussed. Table 3 summarizes the key results at the best constrained locations for each event. Consensus aerosol optical models are developed in section 4.

3.1. On 4 April 2001 (C-130, Twin Otter, *Ron Brown*, and Amami Station)

[43] Figure 1a gives a satellite view of a 400-km-wide swath extending from just north of Oki Island, in the Japan Sea, to beyond Amami Island in the East China Sea south of Japan, at 0211 UTC. The locations of four ACE-Asia platforms at overpass time are labeled, and are listed in Table 1.

3.1.1. Regional Meteorology

[44] The C-130 and Twin Otter were nearly colocated in the vicinity of Oki Island, in a cloud-free region filled with dry air having low aerosol loading. They were under the influence of a high-pressure ridge that extended from a surface anticyclone NW of Shanghai on 2 April up to about 4 km, and elongated somewhat as it moved ESE over the subsequent two days. At the time of satellite overpass, the surface pressure exceeded 1012 hPa over the northern part of the study region. West of the study region, a closed anticyclonic circulation was present well above the mixed layer, extending up to 700 hPa.

[45] Back trajectories (HYSPLIT model, 2002) for the area surrounding Oki Island show that five days previously, the near-surface (500 m) air was located to the NNE, in eastern Mongolia, Manchuria, and the Khabarovsk region of Russia. According to this model, lower tropospheric air (1.5 to 2 km) traveled almost due south across central Siberia and Manchuria, whereas midtropospheric air, at 4–5 km altitude, came from farther west, paralleling the border between Mongolia and Russia where dust sources are common.

[46] The *Ron Brown* was operating under partial cloud south of Kyushu Island and roughly 670 km south of the aircraft; Amami Island, about 340 km SSW of the RB, was under total cloud cover. The clouds were part of a frontal band associated with a low-pressure center that had formed over NE China, near 45°N, 125°E on 1 April, and had moved offshore; at the time of the overpass it was NE of Sakhalin Island.

[47] Frontal passage at the RB was noted at 0900 UTC on 3 April, about 5 hours before overpass time. Back trajectories are similar for the RB and Amami Island sites, and reflect different history from the Oki air mass. The lower tropospheric air above these more southerly locations spent the previous five days over a heavily polluted region that includes Korea, the Yellow Sea and the east coast of China. Back trajectories for midtropospheric levels are from the east, across open areas of the Pacific Ocean.

3.1.2. Sea Surface Conditions

[48] Near-surface winds around Oki Island are constrained by the air speed-ground speed difference during low-altitude, level flight by the C-130 and TO. The winds were low, nominally around 3.4 m s^{-1} at 54 m elevation for the C-130, and 4.0 m s^{-1} at 42 m elevation for the TO, near satellite overpass time. Visual inspection of the ocean supports the calm sea interpretation; low swell and no whitecaps were observed.

[49] Near-surface winds at the *Ron Brown* blew consistently from 30° to 50°E of north, at speeds between 10 and 15 m s^{-1}, within an hour of the overpass. Wave heights were reported at 2–3 m, consistent with the wind speed, and the surface diffuse reflectance, measured aboard the RB by the SIMBAD radiometer, amounted to 0.0046 ± 0.0003 at 560 nm, diminishing to less than 0.0005 at 670 nm, but augmented by whitecaps. At the Oki site, surface diffuse reflectance is slightly higher, on the basis of analysis of SeaWiFS observations of the region and SIMBAD measurements made near the site on 13 April (Table 3).

3.1.3. Aerosol Properties Near Oki Island

[50] In the vicinity of Oki Island, spectral AOT_{col} measured by the AATS-6 aboard the C-130 and the AATS-14 on the TO give a consistent, low-aerosol-optical-depth picture for the region, matching well with the aerosol extinction profiles deduced from the Neph-130 + PSAP-130 system. For example, on two low-level flight legs, the AATS-14 $AOT_{col}(525)$ was 0.153, and its spatial variance was around 4%, about the size of the formal measurement uncertainty. The legs lasted 28 min, began 32 min prior to the satellite overpass, were constrained to elevations between 30 and 51 m, and covered points separated by as much as 53 km, all near Oki Island. The AATS-6 $AOT_{col}(526)$ was within 0.142 ± 0.01 over a 15-min low-level leg, at elevations confined between 47 and 64 m, and covering points separated by 93 km, also near Oki Island. The agreement among these measurements, separated in space and time, speaks to the uniformity of the aerosols in this air mass on scales of tens of kilometers. Since the flight patterns were not designed to uniformly sample an extended area, formal assessment of aerosol air mass variability will be possible with the help of MISR data, once the satellite aerosol retrieval algorithms have been fully validated.

[51] To characterize the total column with a small number of particle types, we define "layers," using minima in the extinction vertical profile, elevations marking rapid changes in particle properties, and levels above which the aircraft did not sample well. The lowest ~50–75 m could not be well observed by the aircraft, but extrapolation to the surface adds negligibly to total column properties in most cases, as can be judged by comparing the AOT(550) uncertainty with the product of the unsampled near-surface region's thickness and $\sigma_{ep}(550)$ for the lowest layer (layer 1). (The $\sigma_{ep}(550)$ is estimated from the quotient of layer 1 AOT and layer 1 vertical extent, given in Table 3 for each case.)

[52] The C-130 flew three vertical profiles, and the TO flew two, within an hour of the MISR overpass; the AATS, Neph-130, and OPC-130 data all indicate that below 4.5 km, two aerosol layers were present, within measurement uncertainties (Figure 2a). Layer 1 has uniform extinction in a well-mixed column between the surface and about 2.0 km elevation; layer 2 extends from about 2.0 km to 3.75 km, with peak extinction near 3 km. Along with total-column and layer spectral AOT, Table 3 gives uncertainty estimates that combine systematic measurement

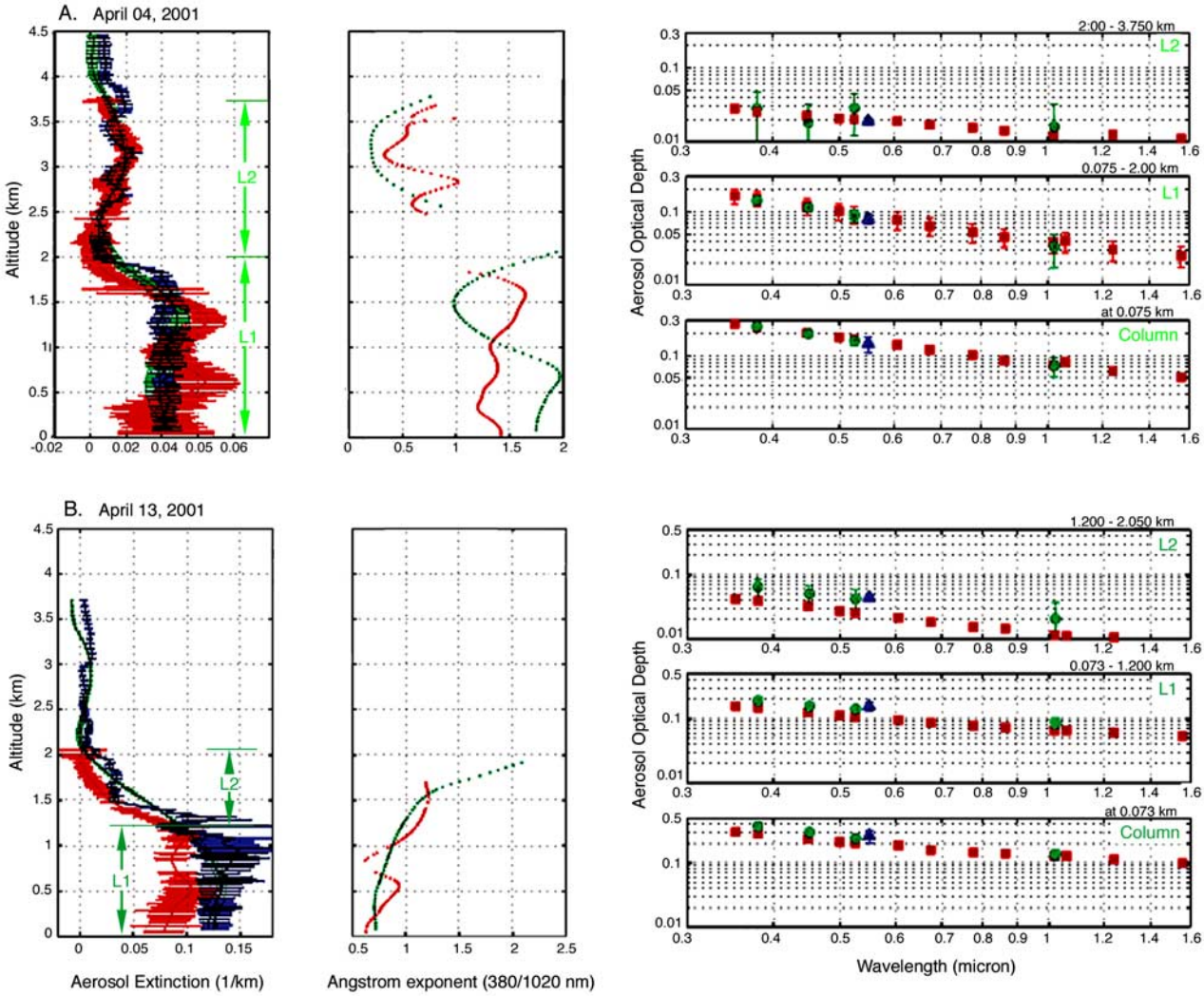

Figure 2. Vertical profiles from the Twin Otter AATS-14, the C-130 AATS-6, and Neph-130 + PSAP-130 instruments. The left panels show 500 nm aerosol extinction as a function of height; the middle panels present A_{ep}(380, 1020). At right are panels showing spectral optical depth for the entire column (bottom) and individual layers in sequence above it. The symbols and plots are color-coded according to the data source: green for AATS-6, red for AATS-14, and blue for Neph-130 + PSAP-130. (a) On 4 April 2001. C-130 data are averages of three profile flights that began at 0002, 0054, and 0154 UTC and lasted about 40 min each. The two profiles contributing to the TO observations began at 0010 and 0125 UTC. The C-130 and TO were separated by between 25.3 and 99.1 km during these profiles. (b) On 13 April 2001. C-130 data are averages of two profiles that began at 0016 and 0105 UTC, the first lasting about 15 min, and the second lasting about 47 min. The TO profiles were taken about 380 km away, beginning at 0042 and 0205 UTC and lasting 29 and 19 min, respectively. (c) On 16 April 2001. Twin Otter AATS-14 data are averages of two profiles that began at 0004 and 0133 UTC and lasted 24 and 28 min, respectively. (d) On 27 April 2001. C-130 AATS-6 and Neph-130 + PSAP-130 data are taken from two profiles that began at 0103 and 0236 UTC. (e) On 2 May 2001. C-130 AATS-6 and Neph-130 + PSAP-130 data taken during the ramped descent that began at 0146 UTC, covering a 104-km region around 33°N latitude, 126°E longitude, east of Jeju Island.

uncertainty with observed variability and other random error sources; in this low-variability case, the uncertainty is dominated by systematic terms. Differences between the AATS-6 and AATS-14 AOT produce standard deviations at least an order of magnitude smaller than the measurement uncertainty given. From AATS, AOT(550) for layers 1 and 2 amount to 0.084 ± 0.019 and 0.020 ± 0.009, respectively; the corresponding values deduced from in situ measurements with Neph-130 are in close agreement: 0.079 ± 0.012 and 0.019 ± 0.002.

[53] Several lines of evidence support the idea that a significant fraction of particles in layer 2 are large, and are probably bright Asian mineral dust, whereas layer 1 is predominantly smaller, darker, pollution particles. The AATS instruments yield ambient A_{ep}(380,1020) of 1.48 in layer 1, indicating small particles, and 0.48 for layer 2

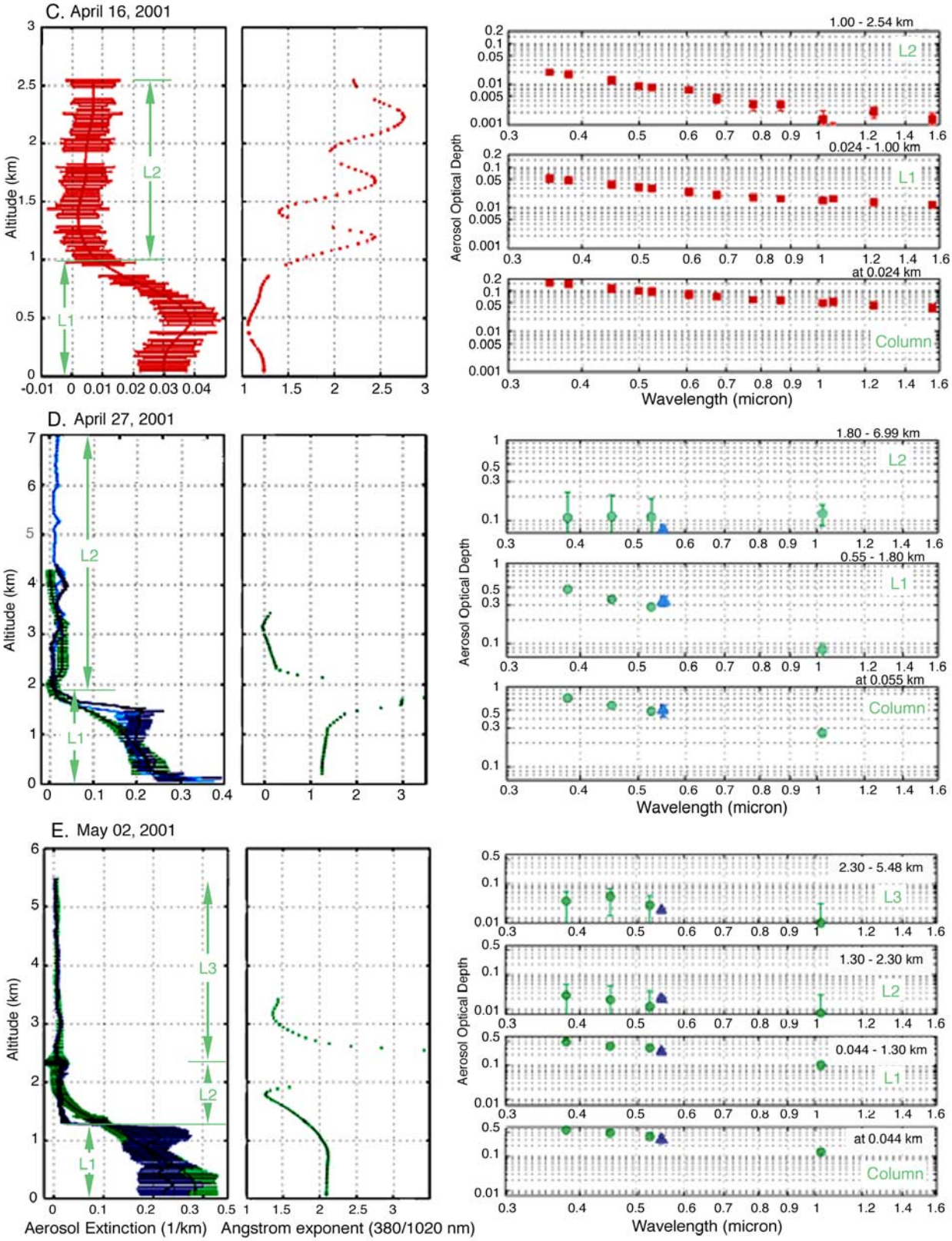

Figure 2. (continued)

(Figure 2a and Table 3). In this environment, large particles in an elevated layer are most likely mineral dust, whereas those near the surface may be sea salt. Neph-130 also identified smaller, darker particles in layer 1 than aloft, producing of $A_{sp}(550,700)$ for layer 1 of 1.52 ± 0.40, SSA(550) of 0.91 ± 0.02, and a submicron fraction AOT(550) of 0.77; the corresponding values for layer 2 are 0.79 ± 0.49, 0.95 ± 0.01, and 0.49 ± 0.06, where the uncertainties are dominated by formal measurement error. These Neph-130 values are dry; the instrument identified the water contribution to ambient $AOT_{sp}(550)$ as about 15% for layer 1 and 5% for layer 2. Having dry particle values from Neph-130 can account for larger Angstrom exponents than those derived from AATS. Neph-130 also found the large particle fraction increased with height in layer 1, suggesting these particles may have precipitated from higher elevations, rather than originating at the ocean surface. OPC-130 and APS-130 optically effective size distributions (section 2.3) elaborate on this picture, finding an accumulation mode in layer 1 having $D_c \sim 0.3 \pm 0.06$ μm and $\sigma \sim 1.44$, along with a weak coarse mode having $D_c \sim 2.9 \pm 0.6$ μm, $\sigma \sim 2.97$, and contributing about 20% to the layer aerosol extinction (Figure 3a). The TO sampled only up to 1.8 km within layer 1, producing an accumulation-mode area-weighted peak around 0.24 μm and a weak coarse mode around 1.8 μm. In layer 2, the C-130 size distributions were somewhat smaller, giving $D_c \sim 0.23 \pm 0.05$ and 2.04 ± 0.41 for the two modes. The upper level coarse-mode extinction is similar (though less well constrained because of lower particle concentration), but the accumulation mode contributes a factor of 4 or 5 less than it does to layer 1.

[54] The in situ sampling suite aboard the TO encountered difficulties during the 4 April flight, but Chem-130 flew legs at three elevations during the two hours subsequent to the satellite overpass (Table 4). Although OC and EC were not reported for this case, Chem-130 results support the conclusion that the boundary layer contained significant pollution (high nss-sulfate), whereas layer 2 was enhanced in calcium, a crustal component associated with mineral dust.

3.1.4. Aerosol Properties at the Southern Sites

[55] MPL-RB showed cirrus near 10 km at satellite overpass time, above an aerosol layer confined to the lowest 2 km. Low signal-to-noise during daylight hours, combined with the boundary and cirrus layer particles, made it difficult to detect any thin, higher-elevation aerosol layers with the lidar. However, there is the suggestion of very thin aerosol between 2 and 4 km in the data, and after sunset, scattering from a thin layer between 6 and 8 km was detected, though too thin to retrieve AOT. For this case, AOT data from Mtps-RB was not obtained because of cloud contamination.

[56] Although high wind and broken cloud made satellite observations difficult, the RB site had a well-defined pollution aerosol layer this day similar to the one deduced at the Oki site. In situ sampling shows two modes, the first having D_c around 0.28 μm, with a range of about 0.02 to 1.2, and the second at 2–3 μm, with a 1–10-μm range, all referenced to 55% RH (Figure 1a). The submicron particles have 30% to 40% mass fraction nss-sulfate, more than 2% EC, and a low SSA(550) of 0.81 (Neph-RB) or 0.86 (NephRH-RB), lower than on subsequent days studied here. The supermicron aerosol was composed of 75 to 84% sea salt, with the majority of the remaining mass being dust, producing

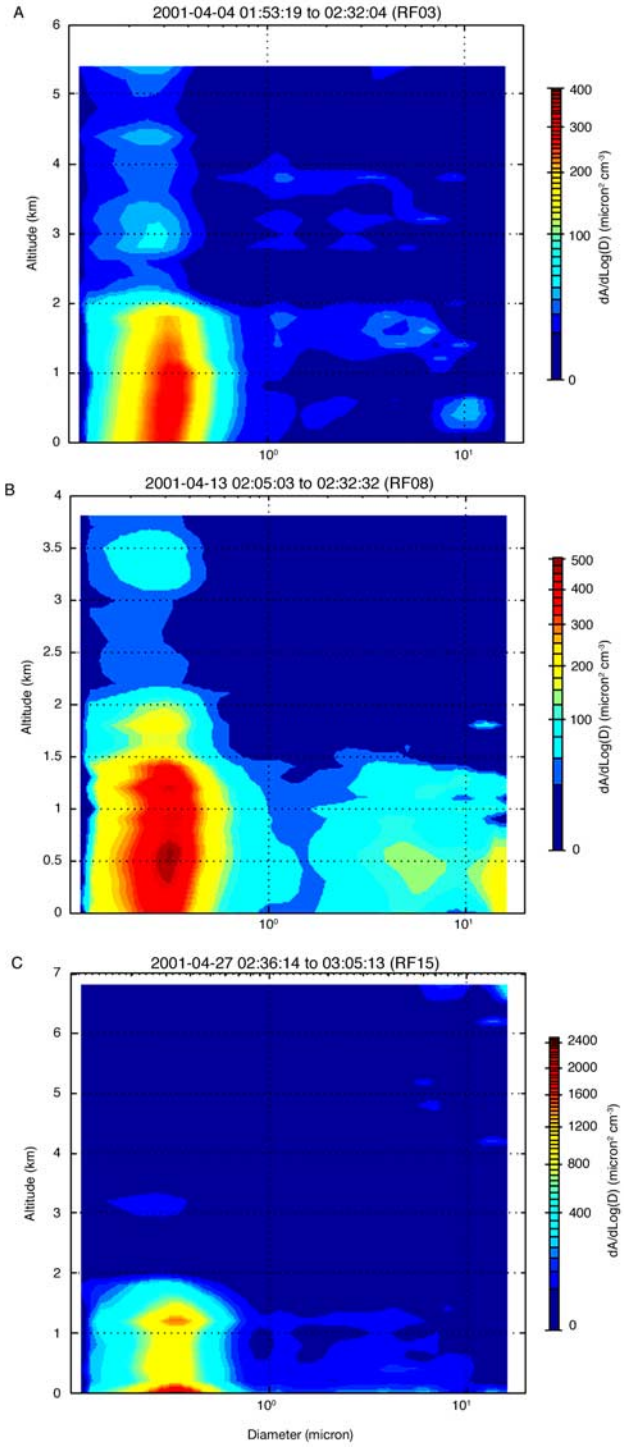

Figure 3. Vertical structure of area-weighted aerosol optically effective size distribution, adjusted to ambient RH (section 2.3) from OPC-130 and APS-130: (a) 4 April 2001, 0153 to 0232 UTC; (b) 13 April 2001, 0205 to 0230 UTC; and (c) 27 April 2001, 0236 to 0305 UTC. Note differences in the scale associated with each color bar.

SSA(550) for the total aerosol of 0.90. NephRH-RB humidograph measurements taken of the near-surface aerosols about 2.5 hours before the overpass exhibited deliquescence and hysteresis, showing a difference between $f(RH)_{sp}$ on the upper and lower branches of the hysteresis loop of 33% at

Table 4. Chem-130 Analyses Near Satellite Overpass Times[a]

Date	Start, UTC	Stop, UTC	Altitude Range, km	nss-Sulfate, $\mu g\ m^{-3}$	NH_4, $\mu g\ m^{-3}$	NO_3, $\mu g\ m^{-3}$	Soluble Ca, $\mu g\ m^{-3}$	OC, $\mu g\ m^{-3}$	EC, $\mu g\ m^{-3}$
4 April	0249	0312	3.18–2.67	3.1 ± 0.6	1.1 ± 0.7	1.9 ± 0.8	1.9 ± 0.9	–	–
4 April	0316	0345	2.30–1.16	5.5 ± 0.5	2.1 ± 0.6	1.9 ±0.6	1.2 ± 0.7	–	–
4 April	0349	0414	0.049–0.628	8.1 ± 0.6	2.9 ± 0.6	1.9 ±0.7	1.2 ± 0.8	–	–
13 April	0116	0145	0.616–1.27	4.9	–	1.0	2.4	4.3 ±1.2	1.2 ± 0.6
13 April	0148	0206	0.032–0.187	5.0	–	1.5	2.1	4.8 ±1.6	2.1 ± 0.9
27 April	0136	0203	0.470	–	–	–	–	20.2 ± 2.4	3.7 ± 0.9
27 April	0206	0235	0.190	–	–	–	–	11.7 ± 1.7	2.5 ± 0.6
2 May	0228	0302	0.044–0.255	8.9 ± 0.5	3.6 ± 0.4	2.3 ± 0.4	1.2 ± 0.5	8.1 ± 1.3	1.5 ± 0.6
2 May	0306	0334	0.456–0.496	8.4 ± 0.5	3.4 ± 0.5	1.8 ± 0.5	0.3 ± 0.6	7.0 ± 1.4	1.2 ± 0.7
2 May	0337	0408	0.935–0.921	4.9 ± 0.4	2.0 ± 0.5	1.7 ± 0.5	0.4 ± 0.6	5.1 ± 1.1	1.1 ± 0.6
2 May	0431	0507	2.836–2.853	–	–	–	–	1.3 ± 0.7	1.3 ± 0.7
2 May	0530	0618	0.247–0.261	11.4 ± 0.6	3.4 ± 0.3	3.7 ± 0.3	0.6 ± 0.4	5.2 ± 0.9	1.3 ± 0.5

[a]Values without error bars are from MOI; all others are from TAS.

RH = 70%. Comparing these results with Neph-RB, the ambient near-surface aerosols were on the hydrated branch of the hysteresis loop. NephRH-RB produced $f(RH)_{sp}$, $A_{ep}(450, 550)$, and SSA were 1.51, 0.81, and 0.90, respectively, at the ambient RH of 63.4%; the low value of A_{ep} may reflect near-surface sea salt.

[57] Farther south, the Amami lidar at satellite overpass time measured a thick cloud layer between 6 and 7 km altitude, in addition to persistent boundary layer cloud at about 1 km, precluding satellite aerosol analysis in this region. The record of photopolarimeter measurements at Amami began about two hours later, giving $AOT_{col}(565)$ around 0.22, and $A_{ep}(443,865) = 0.46$, indicating background amounts of large, sea salt particles that are common at the island station.

3.2. On 13 April 2001 (C-130, Twin Otter, and *Ron Brown*)

[58] Figure 1b gives a satellite view from north of Oki Island to about 31°N latitude in the Pacific Ocean just south of Japan, at 0208 UTC. The locations of three ACE-Asia platforms at the time of overpass are labeled, and are listed in Table 1. The C-130 and RB were nearly colocated in the vicinity of Oki Island, whereas the TO flew NE-SW legs near the surface south of Shikoku, about 380 km away, in the Pacific.

3.2.1. Regional Meteorology

[59] The region appears cloud-free, except for broken cumulus over the intervening land. Back trajectories (HYSPLIT model, 2002) indicate that for the entire experiment region, air at all levels up to 5 km had flowed southeast from central Russia, across east-central Mongolia and the Beijing region of northern China, then over the Yellow Sea and Korean Peninsula during the previous 5 days. An upper level disturbance that moved offshore from China between 30° and 40°N latitude strengthened as it passed the Korean Peninsula. The midlatitude storm that it spawned deepened significantly as it moved northeastward from northern Japan on the previous day. The only other significant weather in the vicinity was a weak midtropospheric system near Beijing. The ambient humidity was somewhat higher to the west than the east of the sampling region, as a developing anticyclone in the southern part of the area brought increasingly moist air in from southwest of Japan.

3.2.2. Sea Surface Conditions

[60] Aboard the RB, the near-surface wind blew consistently from the west, at speeds between 8 and 10 m s^{-1}. Whitecaps were noted. A wind speed of 9 m s^{-1} was deduced for the C-130 in level flight at about 43 m. Surface diffuse reflectance from SIMBAD was 0.007 ± 0.0003 at 550 nm, diminishing to less than 0.001 at 670 nm for whitecap-free patches. Taking into account the effect of whitecaps using a standard, wavelength-independent parameterization [*Monahan and Muircheartaigh*, 1980; *Koepke*, 1984], the total surface albedo is larger, having an estimated value of 0.0085 at 550 nm and 0.0024 at 670 nm. To the south, winds at the Twin Otter were 6 ± 1 m s^{-1} at about 40 m altitude, blowing from the WNW.

3.2.3. Aerosol Properties

[61] The atmosphere as viewed from all platforms contained a low-altitude pollution layer and relatively small but spatially uniform total column AOT. Dust is a more significant component throughout the column on this day than it was on 4 April. For 13 min just before the MISR overflight, starting at 0148 UTC, the C-130 performed a 94-km near-surface leg at 45.5 ± 6 m elevation. During this traverse, AATS-6 recorded AOT(526) of 0.246, with a combined variability and measurement uncertainty of ±0.024. Aboard the RB, AOT(500) was reported as 0.30 ± 0.025 over a 3-min period just before the satellite overpass, nominally greater than the mean AATS-6 value by 0.054. The 45-m elevation difference could contribute only about 0.005, since midvisible aerosol extinction was about 0.12 km^{-1} in the surface layer. Using the AOT spectral slope for layer 1 from Table 3, the RB AOT(500) is reduced to 0.288 at 526 nm, just within the 0.230 to 0.292 range in AOT(526) observed by AATS-6 along its traverse, and supporting the spatial variability estimate of less than ~0.02 on 10-km scales deduced from the AATS; the two instruments took data only a few minutes apart, but were separated spatially by 20–40 km.

[62] Two vertical profiles, obtained before and after the MISR overpass by the AATS-6 and the Neph-130 + PSAP-130, along with those from the MPL-RB, provide a wealth of detail about the column structure (Figure 2b). Two layers were identified. According to the Neph-130 + PSAP-130 and AATS-6, the near-surface layer is a mix of fine pollution particles, contributing 0.57 ± 0.07 to $AOT_{ep}(550)$, with coarse sea salt + mineral dust, extending to 1.2 km (Table 3). It represents a total layer AOT(550) 0.155, with mean SSA(550) 0.92. Ambient $A_{ep}(550)$ from AATS comes to 0.78, indicating a greater fraction of large particles in the boundary layer than on 4 April, and SSA(550) for the submicron fraction is about 0.87 from both Neph-RB and

Neph-130 + PSAP-130. This is at least 0.05 higher than at the RB site on 4 April, and suggests a lower concentration of boundary layer pollution.

[63] The C-130 optical package and AATS-6 identified a second layer of dilute pollution between 1.2 and 2.1 km, having a vertical AOT(550) 0.044, SSA(550) 0.91, and A_{ep}(550) 1.14. The atmosphere between 2.0 and 3.0 km is reported clean, and above this, smaller and somewhat brighter average particles provide an additional 0.065 AOT(550) to the column. Neph-130 + PSAP-130 AOT(550), reconstructed for the lower troposphere, agrees to within 0.02 of the AATS-6 value [*Anderson et al.*, 2003b; *Redemann et al.*, 2003].

[64] MPL-RB confirms this general structure, finding the well-mixed surface layer up to 1 km, dropping to zero at 2 km, and a weak scattering layer between 3 and 3.5 km. The MPL data also indicate a lack of cirrus in the upper troposphere, but show one additional high-altitude aerosol layer, between 7 and 8 km, that appears at 0600 UTC, when the signal-to-noise is higher than it is during the satellite overpass.

[65] Chem-RB sampled the near-surface aerosol layer directly. It determined that the submicron aerosol fraction was somewhat dustier than on 4 April, containing about 15% dust by mass. The supermicron mass fraction was considerably dustier that on 4 April, comprising about 60% of the total sample. 10% to 15% of the supermicron mass was identified as sea salt, as might be expected given the ocean surface conditions. Despite the differences in aerosol mixture, the peaks and widths of the area-weighted modal size distributions were very close to those on 4 April (Figure 1). However, the overall near-surface particle number density was actually higher by about an order of magnitude, because of a nucleation mode having a peak diameter about 0.02 μm, which contributed almost nothing to the area-weighted size distribution.

[66] Chem-130 MOI obtained complimentary data from two samples in the near-surface layer just prior to the MISR overpass (Table 4). Both samples show a moderately polluted air mass having nss-sulfate around 5 $\mu g/m^3$, almost all in the submicron fraction. Dust is somewhat more abundant than on 4 April, even near the surface, in agreement with the other analyses. The C-130 OPC data yield size distributions (Figure 3b) showing patterns relative to 4 April (Figure 3a) that parallel the differences deduced from Neph-130 + PSAP-130. D_c in layer 1 is again about 0.3 μm, and diminishes in layer 2 to about 0.23 μm. From the combined analysis, as described in section 2.3, SSA(550) in layer 1 is 0.89 ± 0.04, and is higher, but less well constrained, in the optically thinner layer 2, where no coarse-mode particles were detected.

[67] A self-consistent analysis of SeaWiFS satellite and SIMBAD near-surface radiometry (Table 2) was performed [*Li et al.*, 2003]. On 13 April a column-averaged mixture of 57.5% Asian dust (by volume), 35% spherical, nonabsorbing, tropospheric particles, and 7.5% soot, was required for the radiative transfer model to agree with both surface and space-based observations over the RB site. Averaged over the column, this mixture produces SSA(443) = 0.834, SSA(555) = 0.831, SSA(670) = 0.836, and SSA(865) = 0.806, lower by 0.07 to 0.1 than the values deduced from the in situ measurements. The difference may reflect uncertainties associated with modeling aerosol vertical distribution and the rough ocean surface for the remote sensing retrieval on this day.

[68] Single-particle SEM provides yet more detail that is helpful in constraining particle models. Results for a filter sample collected on the RB between 0108 and 0308 UTC show a typical, complex mixture of mineral dust, urban pollution products, and sea salt and its reaction products. Relative number concentrations and mean diameters (microns, in parentheses), for particles having geometric diameters from 0.2 to 20 μm are: silicates having little or no aggregated sulfate, 15.8% (4.9), silicates with aggregated sulfate, 6.1% (3.2), completely reacted sea salt (no Cl remaining), 32.5% (0.9), assorted other sulfates and nitrates with metal cations, 14.7% (1.3), and iron oxide, 1.2%. About 10% of particles are carbonaceous, having no other detectable elements, though black carbon particles smaller than 0.5 μm are undercounted by the automated analysis method. The remaining particles are primarily complex aggregates of the above types. Black carbon is also aggregated with the above types, with a frequency that will be quantified in future work. The mean dry diameter of the entire sample is 2.1 μm.

[69] For ACE-Asia mineral dust aerosols sampled on several days, particle shape becomes more complex as particle size increases. A simple two-dimensional shape factor, circularity (equals perimeter^2/(4π*area)) is calculated from SEM images. Each particle type has its own circularity versus diameter relationship. For particles that do not deliquesce, such as silicates without sulfate, the relationship between average diameter and circularity is approximated by a linear regression line having zero intercept at circularity = 1, and slope 0.12. The approximate circularity of an average 10-μm particle comes to 2.2, less than most other dust-bearing ACE-Asia samples analyzed to date. Such details are included loosely in the optical modeling presented here (Table 5; also *Kalashnikova et al.* [2004]).

[70] The TO, at the southerly site, did a 21-km, 6-min traverse at 40-m elevation, starting at 0159 UTC; AOT(525) measured by AATS-14 was tightly constrained to 0.207 ± 0.005. A previous leg, about 17 km to the southwest, had AOT about 10% lower. The aircraft flew near-surface for about an hour prior to the satellite overpass, then spiraled up to about 2.2 km. Two layers appear in the AATS-14 data, one reaching from the surface to 0.7 km, with a peak at 0.5 km, the other extending from about 0.7 to about 1.6 km, with a peak at 1.2 km (Figure 2b). The particle size distribution at ambient RH in the upper layer is essentially monomodal, having an area-weighted peak diameter around 0.22 μm at all levels sampled, close to the 0.25-μm-diameter small mode found near Oki. A tail in the upper layer size distribution, extending to about 7 μm, may hint at a very weak coarse mode. Near the surface, the small mode shows about the same size distribution as in the upper layer, but the supermicron mode is better defined, peaking at about 2.0 μm area-weighted diameter, probably composed of mixed sea salt and dust.

3.3. On 16 April 2001 (Twin Otter, *Ron Brown*, and Gosan Station)

[71] Figure 1c gives a satellite view from Jeju Island south to about 31°N latitude, in the Yellow Sea, at 0217 UTC. The TO was operating in the vicinity of Gosan Station at this time, under cloud-free conditions. The RB

Table 5. Representative Component Aerosol Models[a]

Component Name	D_1, μm	D_2, μm	D_c, μm	σ	n_r	n_i	Submicron Fraction AOT(550)	SSA (558)	SSA (672)	SSA (866)	σ_{ep} (558)	σ_{ep} (672)	σ_{ep} (866)	g	Particle Size/Shape Category
Pollution_0.23_ssa-0.77	0.005	10	0.23 area	1.48	1.47	0.04	1.000	0.769	0.732	0.659	0.025	0.017	0.009	0.573	medium spherical
Pollution_0.23_ssa-0.82	0.005	10	0.23 area	1.48	1.47	0.03	1.000	0.817	0.785	0.721	0.024	0.016	0.009	0.573	medium spherical
Pollution_0.30_ssa-0.83	0.005	10	0.30 area	1.6	1.47	0.035	0.992	0.826	0.811	0.777	0.063	0.046	0.028	0.672	medium spherical
Pollution_0.23_ssa-0.87	0.005	10	0.23 area	1.48	1.47	0.02	1.000	0.871	0.847	0.796	0.023	0.015	0.008	0.572	medium spherical
Pollution_0.30_ssa-0.89	0.005	10	0.30 area	1.44	1.47	0.02	0.999	0.891	0.877	0.844	0.069	0.048	0.026	0.645	medium spherical
Pollution_0.23_ssa-0.91	0.005	10	0.23 area	1.48	1.47	0.014	1.000	0.906	0.888	0.848	0.023	0.015	0.007	0.571	medium spherical
Pollution_0.30_ssa-0.92	0.005	10	0.30 area	1.44	1.47	0.014	0.999	0.922	0.911	0.886	0.069	0.047	0.025	0.643	medium spherical
Sphere_0.05_ssa-1.0	0.005	0.3	0.05 area	1.48	1.43	0	1.000	1	1	1	4.9E-06	2E-06	8E-07	0.053	small spherical
Sphere_0.3_ssa-1.0	0.05	2	0.3 area	1.48	1.43	0	1.000	1	1	1	0.056	0.038	0.020	0.654	medium spherical
Sphere_0.5_ssa-1.0	0.05	2	0.5 area	1.48	1.43	0	1.000	1	1	1	0.351	0.276	0.180	0.742	medium spherical
Asia_Medium_Dust_Grains	0.2	2	1.0 num.	1.5	1.51	0.0011 (672); 7.12 E-4[b] (865)	0.407	0.977	0.991	0.995	2.881	3.082	3.106	0.673	medium nonspherical
Asia_Coarse_Dust	0.2	12	2.0 num.	2	1.51	0.0011 (672); 7.12 E-4 (865)	0.081	0.897	0.949	0.975	2.354	3.363	2.605	0.661	large nonspherical
Sea Salt	0.05	15	3.3 area	3.02	1.48	0	0.231	1	1	1	1.735	1.758	1.783	0.739	large spherical
High_Alt_Sulfate	0.05	10	0.90 num.	1.3	1.43	0	0.819	1	1	1	2.429	2.616	2.44	0.739	medium spherical
Cirrus	6	400	–	–	1.32	0	0.000	1	1	1	967.48	967.48	967.48	0.814	large nonspherical

[a]The area-weighted, lognormal particle size distribution function adopted here for all spherical components is given in equation (3), and their single-scattering phase functions were calculated using a Mie code. Here, n_r and n_i are the real and imaginary parts of the particle refractive index. Wavelength in nanometers is specified in parentheses where appropriate. For medium Asian dust a number-weighted lognormal size distribution was adopted, and a discrete dipole approximation code produced optical properties for a range of shapes and orientations designed to reproduce the observed increase in circularity with particle size [*Kalashnikova et al.*, 2004]. For coarse-mode Asian dust we preformed T-matrix calculations using an area-weighted lognormal distribution having oblate and prolate ellipsoids with a uniform distribution of aspect ratios. Modeling the asymmetry parameter g will generally represent nonspherical particle phase functions poorly for the purpose of calculating MISR multiangle radiances; dust particle phase functions used here are given by *Kalashnikova et al.* [2004]. The high-altitude sulfate model is based on *Wang et al.* [1989].

[b]Read 7.12 E-4 as 7.12×10^{-4}.

was stationed about 200 km to the south, in a region of broken cloud.

3.3.1. Regional Meteorology

[72] The low-level circulation near Gosan was from the south, around a weak center of high pressure centered 470 km to the east. No other regional features directly impacted the meteorology in the study area. At the RB the humid mixed layer was less than 600 m deep, but grew deeper, and was capped with a layer of dry air up to about 3 km prior to the overpass. Winds from the WSW in the layer from 3 to 5 km driven by a trough to the west over China, brought substantial subtropical moisture, increasing the humidity to near saturation by 0300 UTC, accounting for the cloudiness.

[73] Back trajectories (HYSPLIT model, 2002) for the region around Jeju Island indicate air masses having covered the same territory as those for the 13 April study region. Air at all levels up to 5 km flowed southeast from central Russia during the previous five days. The same is true for the RB site, except that above 3 or 4 km, the air apparently took a more southerly route across central China.

3.3.2. Sea Surface Conditions

[74] Surface winds at Gosan were reported to come from the SSW at about 6 m s^{-1}. The TO measured winds from the WSW at about 3.5 ± 0.5 m s^{-1} during low-level flight around overpass time, at 42 ± 2 m altitude. At the more southerly RB location, the near-surface wind blew steadily from the ESE, at about 6 m s^{-1}, producing light whitecaps and swell of 0.2 m.

[75] Surface diffuse reflectance, measured aboard the RB by the SIMBAD radiometer, amounted to 0.0094 ± 0.0004 at 550 nm, and 0.0016 ± 0.0004 at 670 nm. These numbers are higher than at the Japan Sea and Philippine Sea sites for the previous two events, consistent with our knowledge of ocean color derived from SeaWiFS satellite observations. On 15 April, SeaWiFS imagery covered the southern parts of the Korean Strait and the Yellow Sea, into the north part of the South China Sea (31°–34°N latitude; 126°–130°E longitude). The derived marine reflectances were about 0.010, 0.005, and 0.001 at 443, 555, and 670 nm, respectively. They increased slightly to the SW, but greatly to the NW, influenced by outflow from the Yangtze and Yellow rivers. At 34°N and 126°E, values reached 0.04 at 443 and 555 nm and 0.01 at 670 nm.

3.3.3. Aerosol Properties

[76] Aerosol loading was low this day in the vicinity of Jeju Island, consistent with the air having come from regions that are neither major pollution nor dust sources. The Gosan AERONET Sun photometer reported AOT(500) of 0.105 ± 0.006, covering the 2-hour period centered on the MISR overflight, agreeing, within uncertainties, with Sun-Gos, Sunphot-Gos, and with AOT calculated from MPL-Gos. Also at overpass time, the TO flew for 26 min, 42.6 ± 0.3 m above the surface, along a 70-km leg 100 km SE of Jeju Island. The AATS-14 recorded $AOT_{col}(525)$ of 0.103 ± 0.007; adjusting to 500 nm using A_{ep} from Table 3, AOT is 0.098. At the partly cloudy RB site, cirrus contributed to making the AOT both much higher and more variable, registering 0.57 ± 0.08 at 500 nm over a 9-min period about 15 min after the overpass.

[77] Vertical profiles around Jeju show two aerosol layers, one having peak concentration 0.5 km above the surface, the other extending from about 1.2 to 2.7 km (Figure 2c). The AATS-14 vertical profile began about 20 min after the overpass, about 80 km SE of Gosan Station; it lasted 16 min and reached an altitude of 2.5 km. This profile generated a vertical AOT for the lower layer of 0.028 ± 0.001 at 550 nm, 0.006 ± 0.001 for the upper layer (to 2.5 km), and 0.055 above. The MPL-Gos profile shows similar layering, but the magnitudes of the peaks depend on uncertain interpretation of the data in this case. There is no indication of cirrus in the column from either the AATS or MPL-Gos profiles, though even the near-nadir MISR views of the region (Figure 1c), and more so in the steeper views, suggest fairly uniform, subvisible haze over much of the area.

[78] At the more southerly RB site, cirrus was present at 10–12 km at overpass time. MPL-RB identified three distinct aerosol layers, one from the surface to 1.0 km, a second between 1 and 2 km, and a third from 2 to 3 km. Here the peak extinction values are higher than at Gosan, about 0.1 km^{-1} in the surface layer, 0.15 km^{-1} in layer 2, and 0.25 km^{-1} in layer 3, all measured at around 0118 UTC, the closest time to overpass for which data were taken. Over the previous hour, the AOT for the upper two layers increased, whereas the near-surface aerosol remained relatively constant, suggesting a possible relationship to the increasing thickness of the humid mixed layer at the time.

[79] Particle size distributions from two teams at Gosan indicate the surface layer was dominated by an accumulation mode having area-weighted dry diameter peaked between 0.2 and 0.3 μm. The corresponding quantity from the RB was 0.3 μm, but at 55% RH; the TO, at ambient RH and averaged over layer 1, retrieved 0.24 ± 0.03 μm. A 3-μm coarse mode makes a small additional contribution to the size distribution in the boundary layer at all three sites (e.g., Figure 1c). The TO observed accumulation-mode particles in layer 2 with a size distribution also peaked at 0.24 μm, but no appreciable coarse mode. Chem-RB found near-surface particle compositions similar to those on 13 April, though in concentrations lower by a factor of 2 or more. The submicron component contained about 20% mass fraction dust or ash, 30% nss-sulfate, and 15% organics, yielding SSA(550) around 0.88 at 55% RH, whereas the supermicron fraction was dominated by mineral dust, giving a SSA(550) around 0.9. NephRH-RB measurements between 0230 and 0315 UTC show that light scattering and aerosol hygroscopicity were both in the moderate range, with dry σ_{sp} = 34.8 Mm^{-1}, σ_{bsp} = 4.3 Mm^{-1}, and $f(RH = 82\%)_{sp}$ = 2.1. Though there was only slight evidence of deliquescence or crystallization, comparison of results from NephRH-RB and Neph-RB show that the ambient aerosol was again on the hydrated upper branch of the hysteresis loop. $f(RH)$, $A_{sp}(450, 550)$, and SSA(550) were 2.13, 1.21 and 0.96, respectively, at the ambient RH of 84.8%.

[80] Neph-Gos + PSAP-Gos found the extinction was evenly divided between the submicron and supermicron modes at the surface. The submicron mode had SSA(550) of 0.85 and $A_{sp}(450, 700)$ of 2.33 at ambient RH (72.5%), significantly higher than the dry SSA of 0.7. For total aerosol smaller than 10 μm, the SSA(550) was 0.90 and $A_{sp}(450, 700)$ 1.4 at ambient RH, in agreement with values from the RB. Available total column and layer values, from TO measurements, are given in Table 3.

3.4. On 27 April 2001 (C-130, Twin Otter, Amami Station)

[81] Figure 1d gives a satellite view from the Korean Strait in the north, across Kyushu Island, to Amami Island in the East China Sea, at 0219 UTC. The TO was operating in the eastern channel of the Korean Strait, whereas the C-130 performed a circuit across southern Korea that brought it in the vicinity of the TO early in the flight, from about 0100 to 0250 UTC, when it executed a series of east-west legs. Amami Station also appears in the MISR field of view, about 620 km south of the aircraft.

3.4.1. Regional Meteorology

[82] All platforms observed a cover of cirrus at satellite overpass time, which may have been formed by divergent flow at the jet stream level. Weak low-level winds and subsidence in the area around Amami were caused by a broad area of high surface pressure, centered over southern Japan and extending east-west about 3000 km. The ridge weakened above 2 or 3 km. A weak low-pressure feature over central China may have produced the area of significant low-level cloudiness just west of the study region.

[83] Back trajectories (HYSPLIT model, 2002) for the Korean Strait region indicate the air at and above about 4 km had traveled due east over the previous five days, skirting the southern border of Mongolia and crossing the East China Sea south of the Korean Peninsula. Air between 1 and 4 km traveled SE from central Russia, following the Korean coast along the Yellow Sea. Air in the boundary layer traveled nearly due south from the Khabarovsk region of eastern Russia, crossing eastern Manchuria and the Sea of Japan, well east of Korea. The Amami air masses took similar routes, except the lower level air originated farther west, in eastern Mongolia.

3.4.2. Sea Surface Conditions

[84] The TO measured winds from the east of 2 ± 0.5 m s^{-1} at 160 ± 20 m elevation, over a 30-min period that included the satellite overpass. The C-130 also measured low winds, under 1 m s^{-1}, at an elevation around 50 m, and the sea surface appeared glassy calm. No near-surface ocean diffuse reflectivity measurements were made in the region, so for modeling purposes, we adopt values measured in the same area on 4 April (Table 3).

3.4.3. Aerosol Properties

[85] AOT from the AATS instruments was much more variable than on previous days, most likely because of cirrus contributions. The TO executed a 34-min, 52-km east-west traverse just north of latitude 34, starting at 1251 UTC, and staying between 30 and 40 m above the sea surface. During the final 17 min of this traverse, the AATS-14 AOT values ranged from about 0.42 to 0.59 at 525 nm, from 0.36 to 0.53 at 675 nm, and from 0.33 to 0.50 at 865 nm. A second traverse, at an altitude of 157 ± 12 m, beginning about 0227 UTC and lasting 10.5 min, produced AOT ranging from 0.52 to 0.72 at 525 nm. The AATS-6 aboard the C-130 showed similar variability; over the first 5 min of a 28-min traverse in the area around (34°N, 130°E), starting at 0122 UTC, AOT at 526 nm stayed within 0.43 ± 0.04, but then jumped to 0.66. During this period, the aircraft remained within 180 ± 19 m above the surface.

[86] There was less variability at the Amami site. For a 50-min period centered on the satellite overpass, PSR-Am measured AOT(490, 565, 670, 865) of 0.448 ± 0.014, 0.391 ± 0.016, 0.322 ± 0.011, and 0.274 ± 0.006, respectively, along with A_{sp}(443, 865) of 1.00.

[87] Although no lidar was available on any of the platforms this day, the C-130 obtained two vertical profiles over the Korean Strait, the first was completed about one hour prior to the MISR overpass and the second began about 20 min after the overpass (Figure 2d). Here the strength of in situ measurements is evident. Horizontal variability in total AOT makes interpretation of the column AATS data difficult in this case, but the Neph-130 + PSAP-130, along with carefully selected differential optical thickness values from the AATS, provide a consistent picture of the aerosol vertical structure (Table 3). These instruments detected a boundary layer up to 1.8 km that contained within it highly concentrated small particles within 200 m of the surface, and aerosols in low concentration in the free troposphere above, on the basis of measurements up to 6.8 km.

[88] The top of the 200 m sublayer was marked by a sharp RH minimum (30–40%), but there was no increase in coarse-mode concentration toward the surface, which, along with the low surface wind, makes sea salt particles unlikely. Horizontal variations of ±20% in dry light scattering were observed during level legs flown in the boundary layer at about 500 m between the two profiles. Despite the variability, the boundary layer aerosols appeared to have fairly uniform optical properties (Table 3). Multiple, optically thin layers were observed from the top of the boundary layer to 6.8 km, dominated by coarse-mode, nonhygroscopic aerosol (70% of the scattering), apparently dust. Differences in sampling time, convolved with horizontal variability, are likely to account for the differences in layer AOT among the instruments.

[89] Size distributions constrained by the TO particle sizers show accumulation-mode particles having area-weighted mode diameter of about 0.28 ± 0.04 μm, and a weak coarse mode with diameter around 2.8 ± 0.04 μm near the surface, diminishing to about 2.4 ± 0.04 μm higher up. These results were aggregated from measurements taken at four elevations: 100, 200, 500, and 750 m, all in the lower half of layer 1 from the profile analysis (Figure 2d). OPC-130 and APS-130 identify a similar distribution peak for the accumulation mode, up to 1.8 km, but according to these data, the particles are concentrated in two narrow layers, one within a few hundred meters of the surface, and one between about 1.05 and 1.5 km (Figure 3c). The coarse-mode size distribution is less well defined in these data, particularly above 1 km.

[90] The Chem-130 analysis adds detail to the boundary layer characterization, on the basis of two legs flown westward at 494 m and eastward at 180 m, respectively, just prior to and during the MISR overpass. Highly polluted air was found: 20 μg OC/m^3 and 3.7 μg EC/m^3 for the upper leg, and 11.7 OC and 2.2 EC in the lower (Table 4). Also, 1.2 μg Ca/m^3 in the samples supports other indications that dust could have dominated the coarse mode. In the upper leg, OPC-130 found accumulation-mode particles having area-weighted size distributions peaking around 0.35 μm, and APS-130 measured the coarse-mode peak to be near 2.5 μm (Figure 3c). The TO flew eastward at 457 m for 30 min at about the same time; the particle sizers on board also identified an accumulation mode having area-weighted diameter around 0.28 ± 0.04 μm, and a coarse mode having a broad peak centered near 2.4 μm.

[91] Individual particle analysis was performed on samples from the two C-130 legs at 494 and 180 m elevation just before the overpass. At both elevations, more than 80% of the SEM aerosol particles were dominated by mineral dust and mineral dust aggregates. The mean dry diameter for all particles 0.2 μm and larger was about 1.55 μm. Black carbon particles having no other detectable elements were <5% of the 2070 particles larger than 0.2 μm geometric diameter analyzed at both altitudes. Although black carbon particles <0.5 μm in size were undercounted, these samples show less influence from combustion than the samples analyzed on 13 April. These IPA results agree qualitatively with the high submicron SSA(550) obtained by Neph-130 + PSAP-130 in layer 1, but appear to differ from the exceptionally large boundary layer carbon concentrations measured by Chem-130.

[92] For silicates without sulfate, the relationship between mean diameter and circularity can be approximated by a linear regression line having zero intercept at circularity = 1. The corresponding slopes are 0.23 and 0.18 for the 180 m and 494 m samples, respectively, significantly different from the slope of 0.12 for similar particle types in the 13 April sample. These imply an average circularity for 10 μm particles of 3.3 and 2.8, respectively, for the two samples. Having such detail lends confidence to our interpretation of other measurements, and makes it possible to develop increasingly accurate component-particle models (e.g., Table 5) used in interpreting MISR and other satellite observations.

3.5. On 2 May 2001 (C-130 and Gosan Station)

[93] Figure 1e shows the satellite view of Jeju Island and the south end of the Yellow Sea at 0239 UTC. The C-130 was operating in a cloud-free region about 85 km SW of Gosan Station at this time. Starting about 0228 UTC and lasting 1.5 hours, the C-130 flew a series of three stacked, inverted "L"s, to probe atmospheric variability in three dimensions. The base of this pattern ran west 95 km from Gosan over the Yellow Sea toward China, and the stem ran 95 km north from Gosan in the Yellow Sea, parallel to the Korean coast.

3.5.1. Regional Meteorology

[94] Flows in the Jeju region were influenced by a weak, lower tropospheric cyclonic circulation that had formed in place over SW Japan during the previous 24 hours along a stationary trough of low pressure. The disturbance was confined to levels below 5 km, and the northerly winds on its W side were relatively weak over the Yellow Sea. The clouds over the west side of the Yellow Sea seen in the MISR image are low-level stratus that were dissipating at overflight time.

[95] Back trajectories (HYSPLIT model, 2002) indicate that the upper level air traveled from central Russia along the north border of China during the previous few days, roughly as it did on 13 and 16 April, and crossed the Yellow Sea to reach Gosan. Air between 2 and 4 km spent the previous five days along the east coast of China, in the vicinity of Beijing and Shandong province. Below 2 km, the air came from the east, across the Sea of Japan en route to Gosan.

3.5.2. Sea Surface Conditions

[96] Near-surface winds of about 3.4 m s^{-1} were deduced from the C-130, flying at 39 m at overpass time, over calm seas with no whitecaps. Gosan recorded winds from the E-NE at 6 ± 1 m s^{-1}. Since no near-surface ocean diffuse reflectivity measurements were made in the region, for modeling purposes we adopt values measured in the same area on 16 April (Table 3).

3.5.3. Aerosol Properties

[97] The Gosan AERONET Sun photometer reported total column AOT(500) of 0.319 ± 0.02, covering the roughly 2-hour period centered on the MISR overflight, and an instantaneous value of 0.310 within 10 min of the overflight itself, in agreement, within uncertainties, with Sun-Gos and Sunphot-Gos. Sunphot-Gos produced a column-average $A_{ep}(412,862)$ of 1.46 ± 0.02, averaged over two hours around the MISR overpass, compared with 1.37 for AERONET. The C-130 flew 43 ± 3 m above the surface, except during two turns, for about 33 min starting at 0227 UTC. AATS-6 obtained AOT(526) 0.407 ± 0.065 for this entire low-flight period, with extreme values of 0.273 and 0.635. The difference between the C-130 and Gosan values is most likely due to horizontal variability, since the C-130 and Gosan were separated by about 85 km at overpass time. Synoptic observations from MISR, even in the nadir view (Figure 1e), but especially at steeper angles, support the suggestion that thin clouds were present.

[98] A three-layer vertical structure was deduced from the C-130's 53-min ramped descent that started at 6.5 km altitude and reached within 40 m of the surface just before the satellite overpass (Table 3 and Figure 2e). The descent was followed immediately by the three stacked "L"s, at 40 ± 3 m, 456 ± 7 m, and 919 ± 11 m, each lasting about 30 min. Then a ramped ascent to about 3 km, at the extreme north end of the "L" pattern, was performed. This pattern was aimed at refining in situ particle property constraints and at assessing variability.

[99] Aerosols in the vicinity of Jeju Island were characterized by thick, low-level pollution under a relatively aerosol-free upper atmosphere, as might be expected from the trajectory analysis. Surface measurements by Neph-Gos + PSAP-Gos determined the submicron scattering fraction to be 0.84, SSA(550) of 0.95 for sub-10-μm particles, and A_{ep} in the midvisible as 1.88, all at ambient 78% RH. Aerosol extinction under ambient conditions was 0.245 km^{-1}. These are in close agreement with the averaged layer 1 results from AATS-6 and Neph-130 + PSAP-130 (Table 3). Both sets of observations also concluded that over 80% of the scattering was due to moderately hygroscopic, submicron particles.

[100] Between 1.3 km and the top of the boundary layer at 2.3 km, the atmosphere was horizontally stratified, devoid of most aerosols, and humid (RH 70–100%), with scattered clouds. From 2.3 to 6 km the RH dropped below 20%, and the column remained relatively aerosol-free, producing a total AOT(550) of 0.052 from 2.3 km to the top of the atmosphere.

[101] Chem-130 data also identified pollution near the surface, having considerable nss-sulfate, moderate amounts of OC and EC, and little Ca (Table 4). Above 2.8 km, the aerosol is too sparse to allow good chemical analyses. Qualitatively, chemistry derived from Gosan surface sampling agrees with the Chem-130 results. For a sample collected between 0600 UTC on 2 May and 0100 UTC on 3 May, the submicron mode is dominated by sulfate, and organic compounds contributed as well; together they account for about 60% of the total mass loading. Very little dust was observed. However, no particle size distribution data are available for this date.

4. Aerosol Optical Models

[102] In Table 6, synthesis aerosol optical models are given for each layer of each event, derived from the layer-by-layer constraints discussed in section 3. The models are presented as external mixtures of component particles whose properties are listed in Table 5. A "component" is defined as having a single-mode size distribution and uniform composition. The aerosol model for each layer is a mixture of such components. There are three steps in the modeling process. (1) For each event, we used the profile information qualitatively to define layers. (2) For each layer, we then used all available size, composition, and air mass source information discussed in section 3 to help select components and constrain their microphysical properties. (3) Finally, we mixed the selected components externally as required to quantitatively meet up to six optical constraints for that layer (Table 3), allowing the proportions of each component, and the pollution component SSA(550), to vary as needed.

[103] The identities of component aerosols represent the biggest uncertainties in the optical models. They cannot be determined uniquely from optical constraints alone; for example, in most cases we could have matched the layer optical constraints with two spherical components, provided we were free to select their size distributions and SSAs completely arbitrarily. However, we have additional information from the in situ measurements, which is critical for this study, since we expect MISR to exhibit sensitivity to particle sphericity and other microphysical properties [*Kahn et al.*, 2001a], and more generally, because the ability to distinguish anthropogenic from natural aerosols rests on such knowledge.

[104] The component models in Table 5 were derived as follows: We began by adopting size distributions specific to

Table 6. Layer Optical Model Component Fraction AOT(672) for Key Multiplatform Cases[a]

	Date				
	4 April 2001	13 April 2001	16 April 2001	27 April 2001	2 May 2001
Site, platform	Oki, C-130/TO	Oki, C-130/RB	Gosan, TO	Oki, C-130/TO	Gosan, C-130
			Layer 1		
Pollution_0.30_ssa-0.79	–	–	0.47	–	–
Pollution_0.23_ssa-0.80	–	0.45	–	–	–
Pollution_0.30_ssa-0.89	0.67	–	–	–	–
Pollution_0.23_ssa-0.91	–	–	–	0.66	–
Pollution_0.30_ssa-0.92	–	–	–	–	0.73
Asia_Medium_Dust_Grains	0.33	0.2	0.43	0.2	0.27
Asia_Coarse_Dust	–	0.05	0.1	0.14	–
Sea Salt	–	0.3	–	–	–
			Layer 2		
Pollution_0.23_ssa-0.80	–	–	–	0.15	–
Pollution_0.23_ssa-0.86	–	–	0.65	–	–
Pollution_0.23_ssa-0.87	0.22	0.54	–	–	–
Pollution_0.23_ssa-0.91	–	–	–	–	0.38
Sphere_0.05_ssa-1.0	–	–	0.22	–	–
Asia_Medium_Dust_Grains	0.63	0.4	–	0.3	0.62
Asia_Coarse_Dust§	0.15	0.06	0.13	0.15	–
Cirrus	–	–	–	0.4	–
			Layer 3		
Pollution_0.23_ssa-0.86	–	–	–	–	0.45
Asia_Medium_Dust_Grains	–	–	–	–	0.55
			Above Top Layer		
Sphere_0.3_ssa-1.0	0.53	–	–	0.37	0.1
Sphere_0.5_ssa-1.0	–	0.9	0.6	–	0.4
Asia_Medium_Dust_Grains	0.32	–	0.3	0.33	0.3
High_Alt_Sulfate	0.15	0.1	0.1	0.25	0.2
Cirrus	–	–	–	0.05	–

[a]Aerosol component optical models are described in Table 5.

each layer, as measured on 4, 13, and 27 April by APS-130 and OPC-130, adjusted to ambient RH, and those from DMA-TO and APS-TO for 16 and 27 April. Pollution particle models also draw on the RB and Gosan Station boundary layer aerosol characterizations. Segregating the measured size distributions by composition requires additional assumptions (section 2.3), and was explicitly done only for 4 April. So for the purpose of generating optical models to compare with satellite observations, we (1) allow D_c for the pollution component to be either 0.23 or 0.30 μm in layer 1 (Figures 3 and 4). For layer 2, only 0.23-μm pollution particles were needed to satisfy available constraints in all cases. (2) Lacking additional constraints, we let the pollution component's imaginary index of refraction be a free parameter. Having no specific information about the state of absorbing material, we in effect treat any black carbon as being internally mixed in the "pollution" component (see, however, the single-particle analysis discussed in section 3.2). Pollution particles were excluded from the above-the-top layer, but when required to achieve agreement with layer-average optical constraints, (3) we added spherical, nonabsorbing "background" components to upper atmospheric layers.

[105] In the absence of information about SSA at wavelengths other than 550 nm, we chose indices of refraction independent of wavelength for pollution particles; for dust, we internally mixed clay with 1% hematite by volume [*Sokolik and Toon*, 1999; *Kalashnikova et al.*, 2004]. Pollution, sea salt, and background aerosols were modeled as spherical particles, whereas dust was treated as a mixture of irregular shapes that reproduces the circularity relationships discussed in sections 3.2 and 3.4 [*Kalashnikova et al.*, 2004].

[106] To decide when to include pollution particles, Asian dust, and sea salt components in a layer, we used the aircraft-measured chemical abundances (Table 4), RB and Gosan surface sample bulk chemical and IPA analyses, air mass trajectories, and available constraints on SSA at ambient RH from section 3. At the end of the process, we reviewed the derived component mixtures in each case (Table 6) for consistency with the chemical analyses and back-trajectories also found in section 3.

[107] Having selected components, we then solved quantitatively for component fractional abundances separately for each layer, so the calculated values agreed with available layer-average optical constraints to better than the aggregated measurement uncertainty. The optical constraints used (Table 3) are as follows: layer-average $AOT_{ep}(672)$, $AOT_{ep}(558)/AOT_{ep}(672)$, and $AOT_{ep}(866)/AOT_{ep}(672)$ from AATS measurements, and layer average submicron fraction of $AOT_{ep}(550)$, SSA(550), and submicron fraction of SSA(550) from Neph-130 + PSAP-130, all evaluated at ambient RH. For 16 April, SSA and RH constraints come from the TO package.

[108] The results are given in Table 6. They are not unique, primarily because of ambiguities in our knowledge of component properties. However, we have made the simplest assumptions possible consistent with avail-

able constraints. These results are aimed at producing optical models whose accumulated error, when applied to the analysis of satellite observations, is likely to be less that the sum of formal uncertainties given in section 2. For example, optical property differences between internal and external component mixtures are unresolved in available measurements. However, their impact [e.g., *Conant et al.*, 2003] is probably reduced by constraining layer-average quantities with direct observations. Elevations above layer 2 (or for 2 May, layer 3) were sampled remotely, but not directly, by ACE instruments. SAGE II data gives stratospheric $AOT_{ep}(525)$ for the general region as 0.005, and we adopt a standard stratospheric sulfuric acid particle model for this component (*Wang et al.* [1989] and Table 5). We constrain the aerosol component mixture above the top layer sampled to have spectral AOT represented by the difference between the stratospheric AOT and the column AOT above the top layer, as measured by the AATS.

[109] According to Table 6, layer 1 for all events is modeled primarily with a mixture of pollution particles and medium dust, as expected. On 13 April, the windiest day, sea salt makes a significant contribution, and on 16 April, coarse-mode dust is prominent in the Oki site model, a consequence of a relatively small A_{ep} coupled with an observed lack of sea salt, the other large-sized component used in the modeling. We could also obtain a good fit arbitrarily, with generic ''supermicron, nonabsorbing spheres.'' However, we limited the number of components as much as possible, and generic spheres are not invoked in layer 1.

[110] Overall agreement among models and observations is well within measurement uncertainties; Table 7 shows the differences between the model and measurements for each constraint, along with the sizes of the corresponding measurement uncertainties.

[111] Except on 27 April, smaller submicron fractions of AOT(550) correspond to lower A_{ep} in the boundary layer (Table 3), a consistent indication of larger particles from both Sun photometer and nephelometer measurements. However, simultaneously meeting constraints on the submicron fraction of AOT(550), the submicron SSA(550), and the total aerosol SSA(550) places tight restrictions on component properties and abundance. For example, on 13 and 16 April, submicron SSA(550) is low, 0.85 and 0.87, respectively, and the submicron fraction of AOT(550) is close to 0.6 on both days. This means the larger particles must have SSA(550) near the physical limit of unity, if the total SSA(550) is to reach the reported values of 0.90 and 0.92 (Table 3). The supermicron components identified by Chem-RB and other observations (mineral dust, and for 13 April, sea salt as well), have the required high SSA values, and the model adopts submicron pollution particles having SSA(550) of 0.80 ± 0.01 for these cases. On 4 April and 2 May, submicron AOT fraction and SSA are both high in layer 1, so the models contain brighter pollution particles ($SSA(550) = 0.90 \pm 0.02$) and small supermicron fraction in the medium-sized dust mode.

[112] The in situ measurements appear to give differing results on 27 April: Neph-130 + PSAP-130 report a relatively high SSA(550) for both submicron and all particles in layer 1 (Table 3), whereas Chem-130 finds

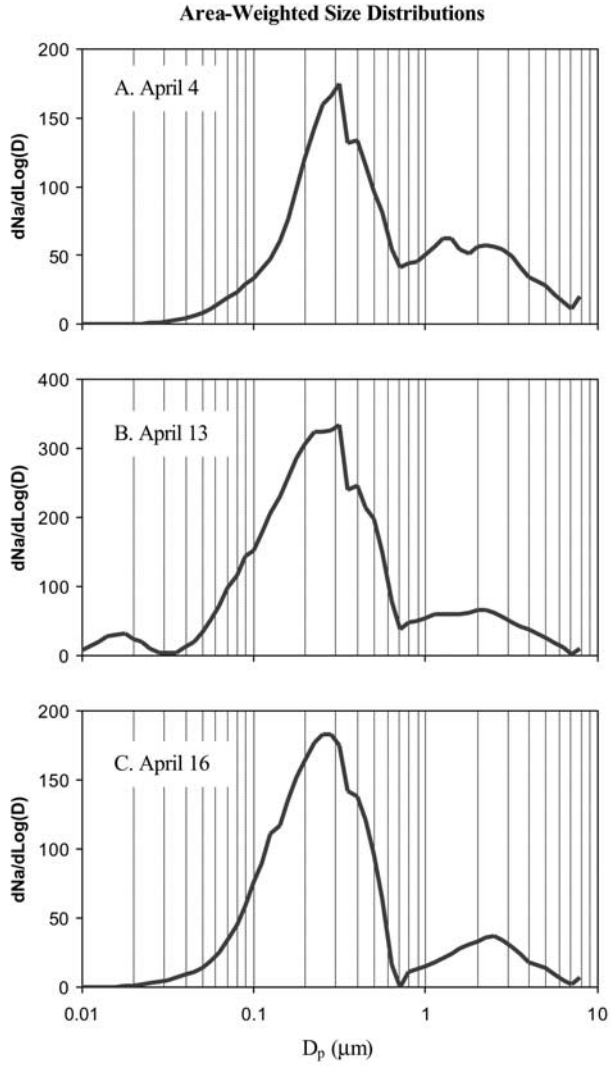

Figure 4. Aerosol area-weighted size distributions at 55% RH in the boundary layer, derived from DMPS-RB, APS-RB, and CPC-RB. Submicron size distributions are reported for geometric diameters, whereas the supermicron distributions are based on aerodynamic diameters, as described in section 2.7: (a) 4 April 2001, (b) 13 April 2001, and (c) 16 April 2001.

both OC and EC abundance at two levels in the boundary layer to be dramatically higher for this event than any other in our sample (Table 4), and chemical analysis from near-coincident TO measurements also show high carbon values [*Mader et al.*, 2003]. In addition, the submicron fraction of AOT(550) is not as high as might be expected given the high A_{ep} value, suggesting particle size distributions different from those on other days, though results from both the C-130 and TO particle sizing instruments do not support this conclusion (see section 3.4). The model adopts a modest amount of coarse dust, along with a large fraction of pollution particles, to reproduce the two quantities. Sampling differences are likely responsible for the apparent measurement discrepancies, since higher horizontal and vertical variability were noted on this day than on others, and we do not have enough information

Table 7. Model-Observation Differences, Layer by Layer, for Each Constraint[a]

	Layer 1		Layer 2		Layer 3		Above Top Layer	
	Model-Observation	Measurement Uncertainty	Model-Observation	Measurement Uncertainty	Model-Observation	Measurement Uncertainty	Model-Observation	Measurement Uncertainty
				4 April 2001				
AOT(550)	−0.002	0.009	−0.002	0.009	–	–	0.000	0.013
AOT(866)	0.000	0.008	0.000	0.008	–	–	0.000	0.012
Submicron AOT(550)	0.003	0.012	0.000	0.002	–	–	–	–
SSA(550)	0.010	0.020	−0.008	0.010	–	–	–	–
				13 April 2001				
AOT(550)	−0.003	0.017	0.001	0.017	–	–	−0.002	0.024
AOT(866)	−0.001	0.016	0.000	0.016	–	–	−0.001	0.023
Submicron AOT(550)	0.005	0.026	0.000	0.005	–	–	–	–
SSA(550)	−0.008	0.020	0.006	0.020	–	–	–	–
Submicron SSA(550)	−0.009	0.030	0.001	0.020	–	–	–	–
				16 April 2001				
AOT(550)	−0.001	0.001	0.000	0.001	–	–	−0.002	0.005
AOT(866)	0.000	0.001	0.000	0.001	–	–	−0.001	0.003
SSA(550)	−0.005	–	–	–	–	–	–	–
Submicron SSA(550)	0.002	–	–	–	–	–	–	–
				27 April 2001				
AOT(550)	−0.013	0.020	0.003	0.072	–	–	−0.001	0.023
AOT(866)	0.001	0.017	−0.014	0.042	–	–	−0.001	0.025
Submicron AOT(550)	0.034	0.043	0.000	0.011	–	–	–	–
SSA(550)	−0.001	0.020	0.003	0.010	–	–	–	–
Submicron SSA(550)	0.004	0.020	0.000	0.030	–	–	–	–
				2 May 2001				
AOT(550)	−0.002	0.054	−0.001	0.023	−0.001	0.024	0.000	0.024
AOT(866)	−0.001	0.033	0.000	0.019	0.000	0.023	0.000	0.023
Submicron AOT(550)	−0.003	0.054	0.000	0.004	0.001	0.002	–	–
SSA(550)	0.007	0.020	0.001	0.010	0.002	0.010	–	–
Submicron SSA(550)	−0.001	0.020	−0.008	0.020	−0.002	0.020	–	–

[a]AOT(672) was matched exactly for each layer.

to justify creating additional component particles for this event.

[113] The AOT for layer 2 is 2–4 times lower than for layer 1 (except on 2 May, when it is almost 20 times lower), even though the second layer is still within 2.5 km of the surface on all but 4 and 27 April. Sampling is more difficult when particle concentrations are low, and optical determinations of aerosol properties are close to uncertainty levels in some cases (Table 3). As expected, we can again produce models that meet the constraints from a mix of dust and pollution, with the addition of cirrus on 27 April, when layer 2 extends to almost 7 km, and small particles on 16 April, a case for which the submicron AOT(550) fraction and A_{ep} are both exceedingly high (Table 3). The tiny 16 April particles were modeled as 0.05-μm-diameter spheres, giving AOT(446) of 0.004. From the back-trajectory analysis, the aerosol source regions for this day were free of unusual dust or pollution components. The tiny particles may be associated with the layer of scattered cloud in the vicinity of Gosan, and probably contribute to the regional haze observed in the MISR images (section 3.3 and Figure 1c). Model results are well within the measurement uncertainties for all events (Table 7).

[114] Only spectral optical depths are used to constrain the aerosol models above the top layer. These constraints are easily met with mixtures of medium spherical nonabsorbing particles, medium dust, and the assumed stratospheric sulfate component. For 27 April we include a small amount of cirrus, which helps reproduce the low value of A_{ep} (Table 3) and reflects the cirrus observed in the study region on that day.

5. Conclusions

[115] Detailed, multiplatform field measurements taken as part of the ACE-Asia campaign constrain to within a few percent the optical properties of atmosphere and surface on five occasions, while the MISR instrument aboard the EOS Terra satellite made column-integrated observations from space. We developed optical models based on a synthesis of field observations, representing environmental snapshots for a range of clean, polluted, and dusty aerosol conditions. These results are summarized in Tables 3, 5, and 6.

[116] We obtained vertical profiles of optical data for all five events (Figures 2a–2e) and defined layers on the basis of changes with height of sampling, aerosol amount, or aerosol type. Our optical models amount to event- and layer-specific mixtures of component particles. Component particle characteristics were derived from the height-resolved particle size and bulk composition information collected. Ambiguities remain in segregating the size distributions by composition. For the purpose of satellite aerosol validation and for other aerosol radiative impact studies, the segregation process is equivalent to assigning spectral SSA values to each component. In this experiment, particle SSA was measured only at 550 nm; having simul-

taneous measurements at one or two additional wavelengths would go a long way toward closing the remaining gaps in environmental characterization for these applications.

[117] To determine aerosol mixtures for each atmospheric layer, we selected components based upon the aggregate of available in situ chemical and physical observations, along with meteorological context. We then solved quantitatively for component particle abundance, constrained by up to six event-specific, layer-average optical parameter measurements, which are presented together with their uncertainties in Tables 3 and 7. The results of this process are not unique, due primarily to ambiguities in the component definitions, but they are based on the simplest assumptions consistent with all the available measurements, and they provide a means of constraining optical models with field measurements taken at a variety of scales.

[118] As expected, aerosols within a few kilometers of the surface during the ACE-Asia study were composed primarily of pollution and Asian dust mixtures. For one event, 13 April, high surface wind added sea salt to the column, and on another, 27 April, cirrus was present, along with greater horizontal spatial variability than on other days. To the degree they were constrained, medium- and coarse-mode particle size distributions varied little among the events studied. However, column AOT changed by more than a factor of 4, the proportion of dust in the lowest atmospheric layer ranged from about 25% (27 April) to 50% (16 April, just after the peak of a major dust event). The amount of absorbing material in the submicron fraction also varied considerably. For modeling purposes, we assumed the absorbing material was internally mixed in the "pollution" component; SSA(550) for this component was around 0.8 on 13 and 16 April, when the near-surface wind crossed Beijing and the Korean Peninsula. For the other events, days when near-surface air originated in eastern Mongolia (4 April) or eastern Korea and the Japan sea (27 April and 2 May), this quantity was close to 0.9.

[119] For layers above 1 or 2 km, AOT was considerably smaller, and observations were less constraining of the models. Among the upper layer models, an interesting result was obtained for 16 April, when 22% of a very small, nonabsorbing component was required to match observations. Although we could not identify any unique aerosol source to link with this component, it may be associated with scattered clouds in the Gosan region. Spectral optical depth measurements, the only constraints available above the highest levels directly sampled by aircraft, were easily fit, though not uniquely, with mixtures of Asian dust and medium-sized nonabsorbing spheres. Upwelling spectral flux measurements, especially at the top of the column sampled by aircraft, and downwelling near-surface flux measurements were unavailable for this study, but could provide valuable integral constraints on such models.

[120] This study also provides insight into the role surface and in situ observations can play in the context of larger-scale satellite aerosol observations and aerosol transport model results. Surface and aircraft remote sensing, nephelometer, and PSAP data produced layer-average optical constraints upon which vertical aerosol structure models were built. We relied on a cascade of more detailed physical and chemical aerosol measurements, down to IPA, to gain confidence in particle size distributions, shapes, and composition, all of which are needed under ambient conditions to create an accurate optical description of the column. Taken together, these measurements provide details about height-resolved particle microphysical properties that cannot be retrieved from any current or anticipated satellite data alone and are beyond the predictive capabilities of current models.

[121] The resulting environmental snapshots can be used for satellite vicarious low-light-level radiometric calibration and aerosol retrieval validation studies, aerosol transport model validation, and regional direct radiative forcing calculations. For satellite radiometric calibration, top-of-atmosphere radiances can be calculated from the surface and atmospheric constraints developed here, and compared directly with radiances measured by the satellite instrument [*Kahn et al.*, 2004]. For aerosol validation, we can, for example, use the MISR research retrieval to determine ranges of aerosol mixtures, components, and amounts that produce simulated MISR radiance values that agree with those observed for each event, to within measurement uncertainty [e.g., *Kahn et al.*, 2001a]. Once the satellite aerosol retrieval algorithms are validated, and the quantitative limitations of the measurements assessed, coincident satellite data can fill in the regional aerosol picture, identifying gradients in aerosol amount and column-averaged properties, and quantifying variability in two dimensions. Similarly, the environmental snapshots can contribute to aerosol transport model validation.

[122] The consistencies in component size distribution and chemical identity among the events studied here suggest that even in this relatively complex aerosol environment, detailed component particle microphysical properties derived from a small number of cases may be more generally representative. A considerable body of literature supports the idea that aerosol types exhibit seasonal and spatial patterns that repeat from year to year, and that microphysical properties of broad classes of mineral dusts, sea salt, biomass burning, pollution, and background particles vary little for many of the largest sources. Satellite observations may be able to map the extent of aerosol air mass types, offering constraints on optical depth and component fractions [e.g., *Kahn et al.*, 2001a] that vary greatly in space and time. Targeted in situ measurements would provide complementary constraints on component properties, filling in a detailed, global picture of aerosol behavior.

[123] Follow-on work to the present study is needed to evaluate the relationship between variability observed in one [e.g., *Anderson et al.*, 2003a, 2003b] and two dimensions, which will help establish practical limits as to how closely satellite and in situ data sets can be combined. Additional effort at applying spatial statistical methods to formally combining aerosol observations taken at multiple spatial [e.g., *Huang et al.*, 2002] and temporal scales would be valuable for this effort as well. Having such results in hand would provide a strong scientific basis for suggesting coordinated surface, in situ, and satellite measurement strategies needed to meet global aerosol monitoring requirements in the future.

[124] **Acknowledgments.** We thank our many ACE-Asia colleagues for their support of this effort, including the ACE-Asia project staff, flight teams, ground teams, and funding agencies. The Joint Office of Science

Support (JOSS), under the University Corporation for Atmospheric Research (UCAR), provided major logistical support for the U.S. portion of this effort. The work of R. Kahn is supported in part by the Climate and Radiation Research and Analysis Program in the Earth Sciences Division of the National Aeronautics and Space Administration, under D. Anderson, the National Oceanographic and Atmospheric Administration Office of Global Programs under J. Levy, and the NASA EOS-MISR instrument program. His work is performed at the Jet Propulsion Laboratory, California Institute of Technology, under contract with NASA. The MISR effort was also assisted by the MISR Team, including David Diner, Barbara Gaitley, Earl Hansen, Duncan McDonald, John Martonchik, and Kyle Miller. This research is a contribution to the International Global Atmospheric Chemistry (IGAC) Core Project of the International Geosphere Biosphere Program (IGBP) and is part of the IGAC Aerosol Characterization Experiments (ACE).

References

Anderson, J. R., P. R. Buseck, T. L. Patterson, and R. Arimoto (1996), Characterization of the Bermuda tropospheric aerosol by combined individual-particle and bulk-aerosol analysis, *Atmos. Environ.*, *30*, 319–338.

Anderson, T. L., and J. A. Ogren (1998), Determining aerosol radiative properties using the TSI 3563 integrating nephelometer, *Aerosol Sci. Technol.*, *29*, 57–69.

Anderson, T. L., R. L. Charlson, D. M. Winker, J. A. Ogren, and K. Holmén (2003a), Mesoscale variations of tropospheric aerosols, *J. Atmos. Sci.*, *60*, 119–136.

Anderson, T. L., S. J. Masonis, D. S. Covert, N. C. Ahlquist, S. G. Howell, A. D. Clarke, and C. S. McNaughton (2003b), Variability of aerosol optical properties derived from in situ aircraft measurements during ACE-Asia, *J. Geophys. Res.*, *108*(D23), 8647, doi:10.1029/2002JD003247.

Bates, T. S., P. K. Quinn, D. J. Coffman, J. E. Johnson, T. L. Miller, D. S. Covert, A. Wiedensohler, S. Leinert, A. Nowak, and C. Neususs (2001), Regional physical and chemical properties of the marine boundary layer aerosol across the Atlantic during Aerosols 99: An overview, *J. Geophys. Res.*, *106*, 20,767–20,782.

Bates, T. S., et al. (2004), Marine boundary layer dust and pollutant transport associated with the passage of a frontal system over eastern Asia, *J. Geophys. Res.*, *109*, D19S19, doi:10.1029/2003JD004094.

Bond, T. C., T. L. Anderson, and D. Campbell (1999), Calibration and intercomparison of filter-based measurements of visible light absorption by aerosols, *Aerosol Sci. Technol.*, *30*, 582–600.

Brechtel, F. J., and S. M. Kreidenweis (2000), Predicting particle critical supersaturation from hygroscopic growth measurements in the humidified TDMA: Part II. Laboratory and ambient studies, *J. Atmos. Sci.*, *57*, 1872–1887.

Brechtel, F. J., S. M. Kreidenweis, and H. B. Swan (1998), Air mass characteristics, total particle concentration and size distributions at Macquarie Island, Tasmania, during the First Aerosol Characterization Experiment (ACE 1), *J. Geophys. Res.*, *103*, 16,351–16,367.

Brock, C. A., et al. (2003), Particle growth in urban and industrial plumes in Texas, *J. Geophys. Res.*, *108*(D3), 4111, doi:10.1029/2002JD002746.

Buzorius, G., A. Zelenyuk, F. Brechtel, and D. Imre (2002), Simultaneous determination of individual ambient particle size, hygroscopicity, and composition, *Geophys. Res. Lett.*, *29*(20), 1974, doi:10.1029/2001GL014221.

Campbell, J. R., D. L. Hlavka, E. J. Welton, C. J. Flynn, D. D. Turner, J. D. Spinhirne, V. S. Scott, and I. H. Hwang (2002), Full-time, eye-safe cloud and aerosol lidar observation at Atmospheric Radiation Measurement Program sites: Instrument and data processing, *J. Atmos. Oceanic Technol.*, *19*, 431–442.

Carrico, C. M., P. Kus, M. J. Rood, P. K. Quinn, and T. S. Bates (2003), Mixtures of pollution, dust, sea salt and volcanic aerosol during ACE-Asia: Radiative properties as a function of relative humidity, *J. Geophys. Res.*, *108*(D23), 8650, doi:10.1029/2003JD003405.

Chin, M., P. Ginoux, S. Kinne, O. Torres, B. N. Holben, B. N. Duncan, R. V. Martin, J. A. Logan, A. Higurashi, and T. Nakajima (2002), Tropospheric aerosol optical thickness from the GOCART model and comparisons with satellite and Sun photometer measurements, *J. Atmos. Sci.*, *59*, 461–483.

Clarke, A. D. (1991), A thermo-optic technique for in situ analysis of size-resolved aerosol physicochemistry, *Atmos. Environ., Part A*, *25*, 635–644.

Clarke, A. D., et al. (2002), INDOEX aerosol: A comparison and summary of chemical, microphysical, and optical properties observed from land, ship, and aircraft, *J. Geophys. Res.*, *107*(D19), 8033, doi:10.1029/2001JD000572.

Clarke, A. D., et al. (2004), Size distributions and mixtures of dust and black carbon aerosol in Asian outflow: Physiochemistry and optical properties, *J. Geophys. Res.*, *109*, D15S09, doi:10.1029/2003JD004378.

Collins, D. R., R. C. Flagan, and J. H. Seinfeld (2002), Improved inversion of scanning DMA data, *Aerosol. Sci. Technol.*, *36*, 1–9.

Conant, W. C., J. H. Seinfeld, J. Wang, G. R. Carmichael, Y. Tang, I. Uno, P. J. Flatau, K. M. Markowicz, and P. K. Quinn (2003), A model for the radiative forcing during ACE-Asia derived from CIRPAS Twin Otter and R/V *Ronald H. Brown* data and comparison with observations, *J. Geophys. Res.*, *108*(D23), 8661, doi:10.1029/2002JD003260.

Delene, D. J., and J. A. Ogren (2002), Variability of aerosol optical properties at four North American surface monitoring sites, *J. Atmos. Sci.*, *59*, 1135–1150.

Deschamps, P.-Y., B. Fougnie, R. Frouin, P. Lecomte, and C. Verwaerde (2004), SIMBAD: A field radiometer for satellite ocean-color validation, *Appl. Opt.*, *43*, 4055–4069.

Diner, D. J., et al. (1998), Multiangle Imaging SpectroRadiometer (MISR) description and experiment overview, *IEEE Trans. Geosci. Remote Sens.*, *36*, 1072–1087.

Diner, D. J., W. A. Abdou, J. E. Conel, K. A. Crean, B. J. Gaitley, M. Helmlinger, R. A. Kahn, J. V. Martonchik, and S. H. Pilorz (2001), MISR aerosol retrievals over southern Africa during the SAFARI-2000 dry season campaign, *Geophys. Res. Lett.*, *28*, 3127–3130.

Doherty, S., T. L. Anderson, and R. J. Charlson (1999), Measurement of the lidar ratio for atmospheric aerosols using a 180°-backscatter nephelometer, *Appl. Opt.*, *38*, 1823–1832.

Dubovik, O., and M. D. King (2000), A flexible inversion algorithm for retrieval of aerosol optical properties from Sun and sky radiance measurements, *J. Geophys. Res.*, *105*, 20,673–20,696.

Dubovik, O., A. Smirnov, B. N. Holben, M. D. King, Y. J. Kaufman, T. F. Eck, and I. Slutsker (2000), Accuracy assessments of aerosol optical properties retrieved from AERONET Sun and sky-radiance measurements, *J. Geophys. Res.*, *105*, 9791–9806.

Dutton, E. G., and B. A. Bodhaine (2001), Solar irradiance anomalies caused by clear-sky transmission variations above Mauna Loa 1957–1999, *J. Clim.*, *14*, 3255–3262.

Dutton, E. G., and J. R. Christy (1992), Solar radiative forcing at selected locations and evidence for global lower tropospheric cooling following the eruptions of El Chichón and Pinatubo, *Geophys. Res. Lett.*, *19*, 2313–2316.

Dutton, E. G., P. Reddy, S. Ryan, and J. J. DeLuisi (1994), Features and effects of aerosol optical depth observed at Mauna Loa, Hawaii: 1982–1992, *J. Geophys. Res.*, *99*, 8295–8306.

Dutton, E. G., J. J. Michalasky, T. Stoffel, B. W. Forgan, J. Hickey, D. W. Nelson, T. L. Alberta, and I. Reda (2001), Measurement of broadband diffuse sollar irradiance using current commercial instrumentation with a correction for thermal offset errors, *J. Atmos. Oceanic Technol.*, *18*, 297–314.

Eck, T. F., B. N. Holben, J. S. Reid, O. Dubovik, A. Smirnov, N. T. O'Neill, I. Slutsker, and S. Kinne (1999), Wavelength dependence of the optical depth of biomass burning, urban and desert dust aerosols, *J. Geophys. Res.*, *104*, 31,333–31,350.

Fernald, F. G. (1984), Analysis of atmospheric lidar observations: Some comments, *Appl. Opt.*, *23*, 653–659.

Fougnie, B., R. Frouin, P. Lecomte, and P.-Y. Deschamps (1999), Reduction of skylight reflection effects in the above-water measurement of marine diffuse reflectance, *Appl. Opt.*, *38*, 3844–3856.

Hogan, T. F., and T. E. Rosemond (1991), The description of the US Navy Operational Global Atmospheric Prediction System's spectral forecast model, *Mon. Weather Rev.*, *119*, 1786–1815.

Holben, B. N., et al. (1998), AERONET: A federated instrument network and data archive for aerosol characterization, *Remote Sens. Environ.*, *66*, 1–16.

Hsu, N. C., J. R. Herman, O. Torres, B. N. Holben, D. Tanre, T. F. Eck, A. Smirnov, B. Chatenet, and F. Lavenu (1999), Comparisons of the TOMS aerosol index with Sun-photometer aerosol optical thickness: Results and applications, *J. Geophys. Res.*, *104*, 6269–6279.

Huang, H.-C., N. Cressie, and J. Gabrosek (2002), Fast, resolution-consistent spatial prediction of global processes from satellite data, *J. Comput. Graph. Stat.*, *11*, 63–88.

Huebert, B. J., T. Bates, P. B. Russell, G. Shi, Y. J. Kim, K. Kawamura, G. Carmichael, and T. Nakajima (2003), An overview of ACE-Asia: Strategies for quantifying the relationships between Asian aerosols and their climatic impacts, *J. Geophys. Res.*, *108*(D23), 8633, doi:10.1029/2003JD003550.

Huebert, B., T. Bertram, J. Kline, S. Howell, D. Eatough, and B. Blomquist (2004), Measurements of organic and elemental carbon in Asian outflow during ACE-Asia from the NSF/NCAR C-130, *J. Geophys. Res.*, *109*, D19S11, doi:10.1029/2004JD004700.

Kahn, R., P. Banerjee, D. McDonald, and D. Diner (1998), Sensitivity of multiangle imaging to aerosol optical depth, and to pure-particle size distribution and composition over ocean, *J. Geophys. Res.*, *103*, 32,195–32,213.

Kahn, R., P. Banerjee, and D. McDonald (2001a), The sensitivity of multiangle imaging to natural mixtures of aerosols over ocean, *J. Geophys. Res.*, *106*, 18,219–18,238.

Kahn, R., P. Banerjee, D. McDonald, and J. Martonchik (2001b), Aerosol properties derived from aircraft multi-angle imaging over Monterey Bay, *J. Geophys. Res.*, *106*, 1977–1995.

Kahn, R. A., B. J. Gaitley, J. V. Martonchik, D. J. Diner, K. A. Crean, and B. Holben (2004), MISR global aerosol optical depth validation based on 2 years of coincident AERONET observations, *J. Geophys. Res.*, doi:10.1029/2004JD004706, in press.

Kalashnikova, O. V., R. Kahn, I. N. Sokolik, and W.-H. Li (2004), Ability of multiangle remote sensing observations to identify and distinguish mineral dust types: 1. Optical models and retrievals of optically thick plumes, *J. Geophys. Res.*, doi:10.1029/2004JD004550, in press.

Kalnay, E., et al. (1996), The NCEP/NCAR 40-Year Reanalysis Project, *Bull. Am. Meteorol. Soc.*, *77*, 437–471.

Kasten, R. (1969), Visibility in the prephase of condensation, *Tellus*, *21*, 631–635.

Kinne, S., et al. (2003), Monthly averages of aerosol properties: A global comparison among models, satellite data, and AERONET ground data, *J. Geophys. Res.*, *108*(D20), 4634, doi:10.1029/2001JD001253.

Klett, D. (1981), Stable analytical inversion solution for processing lidar returns, *Appl. Opt.*, *20*, 211–220.

Kline, J., B. Huebert, S. Howell, B. Blomquist, J. Zhuang, T. Bertram, and J. Carrillo (2004), Aerosol composition and size versus altitude measured from the C-130 during ACE-Asia, *J. Geophys. Res.*, *109*, D19S08, doi:10.1029/2004JD004540.

Knobelspiesse, K. D., C. Pietras, and G. S. Fargion (2003), Sun-pointing error correction for sea deployment of the Microtops II handheld Sun photometer, *J. Atmos. Oceanic Technol.*, *20*, 767–771.

Koepke, P. (1984), Effective reflectance of oceanic whitecaps, *Appl. Opt.*, *23*, 1816–1824.

Lafleur, B. G. (1998), A low turbulence inlet for airborne aerosol sampling, M.S.M.E. thesis, Univ. of Denver, Denver, Colo.

Lee, K. H., H. S. Jung, Y. J. Kim, and C. H. Jung (2002), Size calibration correction for a HAYCO OPC from different aerosol models, progress report, Kwangju Inst. of Sci. and Technol., Kwangju, Republic of Korea.

Li, L.-P., H. Fukushima, R. Frouin, B. G. Mitchell, M.-X. He, I. Uno, T. Takamura, and S. Ohta (2003), Imfluence of submicron absorptive aerosol on Sea-Viewing Wide Field-of-View Sensor (SeaWiFS)-derived marine reflectance during Aerosol Characterization Experiment (ACE)-Asia, *J. Geophys. Res.*, *108*(D15), 4472, doi:10.1029/2002JD002776.

Livingston, J. M., et al. (2003), Airborne sunphotometer measurements of aerosol optical depth and columnar water vapor during the Puerto Rico Dust Experiment, and comparison with land, aircraft, and satellite measurements, *J. Geophys. Res.*, *108*(D19), 8588, doi:10.1029/2002JD002520.

Mader, B. T., R. C. Flagan, and J. H. Seinfeld (2003), Airborne measurements of atmospheric carbonaceous aerosols during ACE-Asia, *J. Geophys. Res.*, *108*(D23), 4704, doi:10.1029/2002JD002221.

Martonchik, J. V., D. J. Diner, R. Kahn, M. M. Verstraete, B. Pinty, H. R. Gordon, and T. P. Ackerman (1998), Techniques for the retrieval of aerosol properties over land and ocean using multiangle imaging, *IEEE Trans. Geosci. Remote Sens.*, *36*, 1212–1227.

Merrill, J. T., and J. Kim (2004), Meteorological events and transport patterns in ACE-Asia, *J. Geophys. Res.*, *109*, D19S18, doi:10.1029/2003JD004124.

Monahan, E. C., and I. O. Muircheartaigh (1980), Optimal power-law description of oceanic whitecap coverage dependence on wind speed, *J. Phys. Oceanogr.*, *10*, 2094–2099.

Murayama, T., et al. (2001), Ground-based network observation of Asian dust events of April 1998 in east Asia, *J. Geophys. Res.*, *106*, 18,345–18,359.

Ohmura, A., et al. (1998), Baseline Surface Radiation Network (BSRN)/WCRP): A new precision radiometry for climate research, *Bull. Am. Meteorol. Soc.*, *79*, 2115–2136.

Quinn, P. K., D. J. Coffman, T. S. Bates, T. L. Miller, J. E. Johnson, K. Voss, E. J. Welton, and C. Neusüss (2001), Dominant aerosol chemical components and their contribution to extinction during the Aerosols 99 cruise across the Atlantic, *J. Geophys. Res.*, *106*, 20,783–20,810.

Quinn, P. K., D. J. Coffman, T. S. Bates, T. L. Miller, J. E. Johnson, E. J. Welton, C. Neusüss, M. Miller, and P. Sheridan (2002), Aerosol optical properties during INDOEX 1999: Means, variabilities, and controlling factors, *J. Geophys. Res.*, *107*(D19), 8020, doi:10.1029/2000JD000037.

Redemann, J., S. J. Masonis, B. Schmid, T. L. Anderson, P. B. Russell, J. M. Livingston, O. Dubovik, and A. D. Clarke (2003), Clear-column closure studies of aerosols and water vapor aboard the NCAR C-130 during ACE-Asia, 2001, *J. Geophys. Res.*, *108*(D23), 8655, doi:10.1029/2003JD003442.

Redemann, J., B. Schmid, J. A. Eilers, R. Kahn, R. C. Levy, P. B. Russell, J. M. Livingston, P. V. Hobbs, W. L. Smith Jr., and B. N. Holben (2004), Suborbital measurements of spectral aerosol optical depth and its variability at sub-satellite-grid scales in support of CLAMS, 2001, *J. Atmos. Sci.*, in press.

Remer, L. A., et al. (2002), Validation of MODIS aerosol retrieval over ocean, *Geophys. Res. Lett.*, *29*(12), 8008, doi:10.1029/2001GL013204.

Russell, P. B., et al. (1993), Pinatubo and pre-Pinatubo optical-depth spectra: Mauna Loa measurements, comparisons, inferred particle size distributions, radiative effects, and relationship to lidar data, *J. Geophys. Res.*, *98*, 22,969–22,985.

Russell, P. B., J. M. Livingston, P. Hignett, S. Kinne, J. Wong, and P. V. Hobbs (1999), Aerosol-induced radiative flux changes off the United States mid-Atlantic coast: Comparison of values calculated from sunphotometer and in situ data with those measured by airborne pyranometer, *J. Geophys. Res.*, *104*, 2289–2307.

Sano, I., S. Mukai, Y. Okada, B. N. Holben, S. Ohta, and T. Takamura (2003), Optical properties of aerosols during APEX and ACE-Asia experiments, *J. Geophys. Res.*, *108*(D23), 8649, doi:10.1029/2002JD003263.

Schmid, B., et al. (2000), Clear sky closure studies of lower tropospheric aerosol and water vapor during ACE-2 using airborne sunphotometer, airborne in-situ, space-borne, and ground-based measurements, *Tellus*, *Ser. B*, *52*, 568–593.

Schmid, B., et al. (2003a), Column closure studies of lower tropospheric aerosol and water vapor during ACE-Asia using airborne Sun photometer, airborne in situ and ship-based lidar measurements, *J. Geophys. Res.*, *108*(D23), 8656, doi:10.1029/2002JD003361.

Schmid, B., et al. (2003b), Coordinated airborne, spaceborne, and ground-based measurements of massive, thick aerosol layers during the dry season in southern Africa, *J. Geophys. Res.*, *108*(D13), 8496, doi:10.1029/2002JD002297.

Sheridan, P. J., D. J. Delene, and J. A. Ogren (2001), Four years of continuous surface measurements from the Department of Energy's Atmospheric Radiation Measurement Program Southern Great Plains Cloud and Radiation Testbed site, *J. Geophys. Res.*, *106*, 20,735–20,747.

Smirnov, A., B. N. Holben, T. F. Eck, O. Dubovik, and I. Slutsker (2000), Cloud screening and quality control algorithms for the AERONET data base, *Remote Sens. Environ.*, *73*, 337–349.

Sokolik, I. N., and O. B. Toon (1999), Incorporation of mineralogical composition into models of the radiative properties of mineral aerosol from UV to IR wavelengths, *J. Geophys. Res.*, *104*, 9423–9444.

Spinhirne, J. D., J. Rall, and V. S. Scott (1995), Compact eye-safe lidar systems, *Rev. Laser Eng.*, *23*, 26–32.

Sugimoto, N., I. Matsui, Z. Liu, A. Shimizu, K. Asai, K. Yoneyama, and M. Katsumata (2001), Latitudinal distribution of aerosols and clouds in the western Pacific observed with a lidar on board the research vessel *Mirai*, *Geophys. Res. Lett.*, *28*, 4187–4190.

Tang, I. N., and H. R. Munkelwitz (1991), Simultaneous determination of refractive index and density of evaporating solution droplets, *Aerosol Sci. Technol.*, *15*, 201–207.

Wang, J., et al. (2003a), Clear-column radiative closure during ACE-Asia: Comparison of multiwavelength extinction derived from particle size and composition with results from Sun photometry, *J. Geophys. Res.*, *108*(D23), 4688, doi:10.1029/2002JD002465.

Wang, J., R. C. Flagan, and J. H. Seinfeld (2003b), A differential mobility analyzer (DMA) system for submicron aerosol measurements at ambient relative humidity, *Aerosol. Sci. Technol.*, *37*(1), 46–52.

Wang, P.-H., M. P. McCormick, T. J. Swissler, M. T. Osborn, W. H. Fuller, and G. K. Yue (1989), Inference of stratospheric aerosol composition and size distribution from SAGE II satellite measurements, *J. Geophys. Res.*, *94*, 8435–8446.

Welton, E. J., and J. R. Campbell (2002), Micro-pulse lidar signals: Uncertainty analysis, *J. Atmos. Oceanic Technol.*, *19*, 2089–2094.

Welton, E. J., et al. (2000), Ground-based lidar measurements of aerosols during ACE-2: Instrument description, results, and comparisons with other ground-based and airborne measurements, *Tellus*, *Ser. B*, *52*, 635–650.

Welton, E. J., J. R. Campbell, J. D. Spinhirne, and V. S. Scott (2001), Global monitoring of clouds and aerosols using a network of micro-pulse lidar systems, in *Lidar Remote Sensing for Industry and Environmental Monitoring*, edited by U. N. Singh, T. Itabe, and N. Sugimoto, *Proc. SPIE*, *4153*, 151–158.

Welton, E. J., K. J. Voss, P. K. Quinn, P. J. Flatau, K. Markowicz, J. R. Campbell, J. D. Spinhirne, H. R. Gordon, and J. E. Johnson (2002), Measurements of aerosol vertical profiles and optical properties during INDOEX 1999 using micropulse lidars, *J. Geophys. Res.*, *107*(D19), 8019, doi:10.1029/2000JD000038.

Willeke, K, and P. A. Baron (1993), *Aerosol Measurement: Principles, Techniques, and Applications*, 876 pp., Van Nostrand Reinhold, New York.

Yoon, S. C., and J. G. Won (1998), Monitoring of atmospheric aerosols in Seoul using a micro pulse lidar, in *19th International Laser Radar Conference, NASA Conf. Publ., NASA/CP-1998-207671/PT1*, 83–85.

Zelenyuk, A., and D. Imre (2001), A new single-particle laser-ablation time-of-flight mass spectrometer for size-resolved composition measurements of ambient particulate matter, paper presented at the Annual Meeting of the American Association for Aerosol Research, Portland, Oreg.

J. Anderson, Department of Mechanical and Aerospace Engineering, Arizona State University, University Boulevard, Tempe, AZ 85287, USA. (janderson@asu.edu)

T. L. Anderson and S. J. Doherty, Department of Atmospheric Sciences, University of Washington, Seattle, WA 98195, USA. (tadand@atmos.washington.edu)

T. Bates and P. Quinn, NOAA PMEL, 7600 Sand Point Way NE, Seattle, WA 98115, USA. (tim.bates@noaa.gov; quinn@pmel.noaa.gov)

F. Brechtel, Brechtel Manufacturing, Inc., 1789 Addison Way, Hayward, CA 94544, USA. (fredb@bnl.gov)

C. M. Carrico, Department of Atmospheric Science, Colorado State University, Fort Collins, CO 80523, USA. (carrico@lamar.colostate.edu)

A. Clarke, S. Howell, B. Huebert, and C. McNaughton, Department of Oceanography, University of Hawaii, 1000 Pope Road, Honolulu, HI 96822, USA. (tclarke@soest.hawaii.edu; showell@soest.hawaii.edu; huebert@hawaii.edu; cameronm@soest.hawaii.edu)

E. Dutton and A. Jefferson, NOAA CMDL, 325 Broadway, Boulder, CO 80305, USA. (edutton@cmdl.noaa.gov; anne.jefferson@noaa.gov)

R. Flagan and J. Seinfeld, Department of Chemical Engineering, California Institute of Technology, 1200 E. California Boulevard, Pasadena, CA 91125, USA. (flagan@caltech.edu; seinfeld@caltech.edu)

R. Frouin, Scripps Institution of Oceanography, University of California at San Diego, 8605 La Jolla Shores Drive, La Jolla, CA 92037, USA. (rfrouin@ucsd.edu)

H. Fukushima, School of High-Technology for Human Welfare, Tokai University, 317 Nishino, Numazu, 410-0395, Japan. (hajime@fksh.fc.u-tokai.ac.jp)

B. Holben and E. J. Welton, NASA Goddard Space Flight Center, Greenbelt, MD 20771, USA. (brent@aeronet.gsfc.nasa.gov; welton@virl.gsfc.nasa.gov)

H. Jonsson, Center for Interdisciplinary Remotely Piloted Aircraft Studies (CIRPAS), Naval Postgraduate School, 3240 Imjin Road, Hangar #510, Marina, CA 93933, USA. (hjonsson@nps.navy.mil)

R. Kahn, O. Kalashnikova, and W.-H. Li, Jet Propulsion Laboratory, California Institute of Technology, 4800 Oak Grove Drive, Pasadena, CA 91109, USA. (ralph.kahn@jpl.nasa.gov; olga.v.kalashnikova@jpl.nasa.gov; wli@sdsio-mail.jpl.nasa.gov)

J. Kim, Meteorological Research Institute, Korea Meteorological Administration, 460-18 Shindaebang-Dong, Dongjak-gu, Seoul, 156-720, South Korea. (jykim@metri.re.kr)

S.-W. Kim, J.-G. Won, and S.-C. Yoon, School of Earth and Environmental Sciences, Seoul National University, San 56-1, Shillim-dong, Kwanak-gu, Seoul 151-742, South Korea. (kimsw@air.snu.ac.kr; wonjg@air.snu.ac.kr; yoon@snu.ac.kr)

P. Kus and M. Rood, Department of Civil and Environmental Engineering, University of Illinois at Urbana-Champaign, 205 N. Mathews Avenue, Urbana, IL 61801, USA. (pinarkus@uiuc.edu; mrood@uiuc.edu)

J. M. Livingston, SRI International, 333 Ravenswood Avenue, Menlo Park, CA 94025-3453, USA. (jlivingston@mail.arc.nasa.gov)

J. Merrill, Graduate School of Oceanography, University of Rhode Island, South Ferry Road, Narragansett, RI 02882, USA. (jmerrill@boreas.gso.uri.edu)

S. Mukai and I. Sano, Faculty of Science and Technology, Kinki University, Higashi-Osaka, 577-8502, Japan. (mukai@im.kindai.ac.jp; sano@im.kindai.ac.jp)

T. Murayama, Faculty of Marine Engineering, Tokyo University of Marine Science and Technology, 2-1-6 Etchujima, Koto-ku, Tokyo, 135-8533, Japan. (murayama@ipc.tosho-u.ac.jp)

T. Nakajima, Center for Climate System Research, University of Tokyo, 4-6-1 Komaba, Meguro-ku, Tokyo, 153-8904, Japan. (teruyuki@ccsr.u-tokyo.ac.jp)

J. Redemann and B. Schmid, Bay Area Environmental Research Institute, 560 3rd Street West, Sonoma, CA 95476, USA. (redemann@atmos.ucla.edu; bschmid@mail.arc.nasa.gov)

P. Russell, NASA Ames Research Center, MS 245-5, Moffett Field, CA 94035, USA. (philip.b.russell@nasa.gov)

N. Sugimoto, Atmospheric Environment Division, National Institute for Environmental Studies, 16-2 Onogawa, Tsukuba, Ibaraki, 305-0053, Japan. (nsugimot@nies.go.jp)

J. Wang, Atmospheric Science Division, Brookhaven National Laboratory, P. O. Box 5000, Upton, NY 11973-5000, USA. (jian@bnl.gov)